Slap!

Developing Hybrid Acousto-Optic Systems for Wavelength Conversion

Maxwell Gordon Drimmer

Mentor: Dr. Igor Marinković

Advisor: Prof. Dr. Simon Gröblacher

A thesis presented for the degree of

Master of Science

Faculty of Applied Sciences — Faculteit Technische Natuurwetenschappen

Delft University of Technology — Technische Universiteit Delft

June 2020

Abstract

The defining challenge of connecting NISQ quantum computers over large distances is efficient microwave to optical transduction. In this work, we demonstrate a new platform for piezo-optomechanical conversion by combining a crystalline silicon nanobeam photonic crystal cavity and a suspended thin-film lithium niobate acoustic resonator. The goal is to combine the excellent optomechanical properties of the silicon nanobeam cavity with coherent excitations in a piezoelectric resonator in order to achieve large effective coupling between the microwave excitation and the optical cavity. In order to fabricate this hybrid silicon-on-lithium niobate device, we explore a technique termed 'slapping' where a loosely connected suspended nanostructure is patterned such that a tapered optical fiber can be used to rip it away and place it in an arbitrary location on another chip. We report a single photon optomechanical coupling rate $g_0 = 5.1$ kHz and a single photon microwave to optical efficiency of $\eta_{\mu \to o} = 6.1 \times 10^{-6}$ at $25 \mu W$ of input optical power in a device limited by a suboptimal optical interface.

I would like to acknowledge my mentor Igor Marinković and my advisor Simon Gröblacher. I've learned so much from you and I cannot express enough gratitude for the time and effort you spent working with me. I'm graduating with enthusiasm for research and confidence in myself, and I thank you both for that.

I also recognize the members of the Gröblacher Lab for their help throughout this process, especially Moritz Forsch, Niccolo Fiaschi for their assistance in editing this manuscript and Bas Hensen and Rob Stockill for their constant stream of valuable experimental advice. I also want to acknowledge Rodrigo Benevides, Jingkun Gao, Ulderico Filippozzi, and Fred Hijazi for their help troubleshooting experimental details. Special thanks to Andreas Wallucks for allowing me to endlessly chat with Igor in his office.

Finally, I am grateful to those who support me, especially Caren Yusem, Alan Drimmer, Clara Drimmer, Hanna Gohlke, Jack Herrera, Emily Lemmmerman, Sienna White, and Buzz Ruttenburg.

Contents

The work presented in this thesis was a collaboration between the author and his mentor, Igor Marinković, carried out between June 2019 and March 2020. Credit for the concept of slapping is due to Dr. Marinković. The fabrication and experiment were performed together until Dr. Marinković departed in November 2019, after which the author continued fabrication and experimental work through the project's completion.

Introduction

One long term goal of Quantum Information Science (QIS) is to connect distant quantum computers in order to create a quantum internet capable of cryptographically secure quantum communication, quantum metrology, and distributed quantum computation [1–4]. In the era of Noisy Intermediate-Scale Quantum (NISQ) technologies [5] this means we are interested in linking together quantum information processors, which consist of superconducting microwave circuits at millikelvin temperatures [6, 7]. There is no way to transmit microwave photons over long distances without ruinous losses, so the microwave qubits inside of dilution refrigerators must be efficiently converted into 'flying qubits' that can enter and exit the refrigerator and travel long distances without decohering [8]. Optical photons are an ideal candidate because they travel at the speed of light and suffer minimal decoherence due to their high frequency. Furthermore, photons with wavelengths around 1550 nanometers can propagate with ultra-low losses in existing worldwide fiber-optic networks, thereby taking advantage of the technology and infrastructure developed by the telecommunications industry.

A NISQ era quantum internet will consist of superconducting quantum processors connected to a telecom-frequency quantum network [9]. Therefore, a method of bidirectional conversion between microwave-frequency photons and telecom-frequency photons must be developed. An additional requirement is quantum efficiency - that is, each microwave photon should be deterministically converted to exactly one optical photon (and vice versa) [1]. This physics problem, also called "quantum wavelength conversion" or "quantum microwave to optical transduction," has been a defining challenge in QIS for the past decade. The large frequency difference between GHz microwaves and THz optics generally requires engineering a highly nonlinear system with strong, efficient interactions - no easy task [10–12].

Direct, electro-optic strategies suffer from low interaction strengths, as it is difficult to localize optical and microwave fields in small enough volumes for efficient transduction [13]. Cold atomic systems (or atom-like systems) have large optical non-linearities which can be used in a three- or four- (or more) wave mixing scheme to facilitate coherent conversion, but these systems are difficult to incorporate with microwave circuits [14, 15]. Instead of direct conversion one can also use an intermediate system that simultaneously couples to optical and microwave fields, usually a bosonic oscillator. While magnon-based conversion

is also being explored, the most successful conversion experiments to date incorporate a mechanical oscillator [11,12]. These experiments consist of a double swap operation between two disconnected resonators linked by an intermediate resonator, as proposed by [16, 17]. Typically, a strong pump detuned from an optical cavity is modulated by a mechanical resonator, the state of which depends on the state of the microwave resonator. This can be implemented by systems that co-localize an optical cavity mode with a mechanical resonator cooled close to its quantum ground state and electrically connected to a microwave circuit. A non-exhaustive collection of these experiments is found in Refs. [18–26].

The task of mechanically-mediated microwave to optical transduction can be broken down into the subproblems of electromechanical and optomechanical conversion. In the last few years, progress towards efficient electromechanical conversion was achieved by connecting microwave qubits to piezoelectric acoustic resonators. Most notably, Refs. [27–29] swapped excitations from a microwave qubit to mechanical oscillators inspired by commercial acoustic devices. We attempt to build on these results by design an optical cavity capable of interfacing with the same piezo-acoustic resonators in order to build a system capable of quantum wavelength conversion. This is the primary motivation for the development of quantum-efficient piezo-optomechanical transducers.

The field of optomechanics has successfully engineered a variety of systems that co-localize mechanical and optical modes [30]. We focus on the one-dimensional Optomechanical Crystal (OMC) nanobeam because it has been studied extensively, works at telecom frequencies, and can be designed lithographically. These structures consist of a photonic crystal defect cavity patterned into nanobeam and are designed to maximize overlap between an optical mode of the cavity and the breathing mode of the nanobeam, resulting in impressive optomechanical interaction rates (> 1 MHz) [31]. Furthermore, the mechanical mode can be designed in the gigahertz frequency range and can thus be cooled to its quantum ground state of motion (either actively, by laser cooling as in Ref. [32] or passively, cryogenically as in Ref. [33]). Originally developed in silicon and silicon nitride, this design is robust and has been reproduced in piezoelectric materials such as gallium arsenide [34], aluminum nitride [18], lithium niobate [35], and gallium phosphide [36, 37].

One challenge of using photonic crystal cavity nanobeams for piezo-optomechanical transduction is that the mechanical breathing mode is located in the center of a sensitive photonic structure and cannot be directly connected to a microwave circuit. There have

been two strategies to overcome this. Some efforts attempt to focus propagating phonons into the nanobeam where they can interact with the optomechanical cavity [20, 23, 24]. Alternatively, one can design a mechanical 'supermode,' a mode where separated regions of the nanobeam are displaced at once. Optomechanical devices with hybrid mechanical modes of a block piezo-resonator and a nanobeam can simultaneously interface with a microwave circuit and an optical cavity, as demonstrated in Refs. [18, 38, 39].

While these approaches are exciting, most run into the same problem - it isn't clear which piezoelectric material has the best properties for quantum wavelength conversion. The final device must be able to efficiently couple to qubits and support high Q factor mechanical modes and thus needs to utilize a highly piezoelectric element. Materials typically fall into one of two groups: those with good optomechanical properties (i.e. absorption coefficients, refractive indices, etc.) and materials with good piezoelectric properties (i.e. piezoelectric and elasticity coefficients). Unfortunately, materials that exhibit strong piezoelectric attributes typically have poor optical properties that limit optical efficiency and optomechanical coupling rate. This means that any monolithic device (made of a single material) will ultimately require a compromise between optomechanical and electromechanical performance.

Luckily, we are not limited to using a single material. A system that combines a good piezoelectric material with a good optomechanical material is an excellent candidate to resolve this issue. This thesis is an investigation of a hybrid technique for piezo-optomechanical transduction. It is organized into three chapters:

Chapter 1 We develop 'slapping,' a method for rapidly prototyping a composite system. Slapping is a 'pick-and-place' process where structures patterned on one chip are ripped off and placed onto another chip using a tapered optical fiber.

Chapter 2 We engineer and fabricate thin film lithium niobate electromechanical resonators suited for wavelength conversion.

Chapter 3 We design and test a transducer consisting of a silicon optomechanical crystal slapped onto a lithium niobate electromechanical resonator.

Chapter 1

Slapping

The goal of this thesis is to explore a new platform for OMC-based transduction. We argue that multi-material approaches to wavelength conversion have an advantage over monolithic ones and investigate a technique called **slapping** to combine lithium niobate and crystalline silicon nanostructures. The slap procedure consists of ripping structures away from one chip with a tapered optical fiber and placing them down at a specific location on another chip. In this chapter, we elaborate on our optimized, high-precision procedure and list some of the limitations of our 'pick-and-place' method. Finally, we suggest improvements to be implemented in future slapping research.

1.1 Motivation

We begin with a brief introduction of the 1-D photonic crystal cavity. One method of measuring these devices is by touching a tapered optical fiber to a coupler which guides light into the nanophotonic structure. The silica fiber can adhere quite strongly to these devices, which gave inspired some researchers to rip photonic structures off of the chip they were fabricated on. Inspired by the hybrid platforms developed for integrated silicon photonic circuits, we will take this idea further by using an optical fiber to pick up *and slap down* nanostructures.

1.1.1 Photonic Crystal Cavities

Our understanding of the behavior of light in periodic structures is crucial to the study of optics. When the minimum feature size (MFS) of available nanofabrication technologies was pushed low enough to pattern sub-wavelength features in solid-state structures, self-similar devices called 'photonic crystals' were developed. Solving Maxwell's Equations in periodic elliptical holes yields a range of wavelengths for which propagation of optical modes is forbidden; this structure is called a Distributed Bragg Reflector (DBR) [40]. The design, shown in Fig. 1.1 (a), is a one-dimensional array of mirror cells where the geometries of a few 'defect cells' are adiabatically altered. The resulting optical cavity supports standing waves in the defect region surrounded by DBRs acting as mirrors. This structure is known as a 'photonic crystal cavity.'

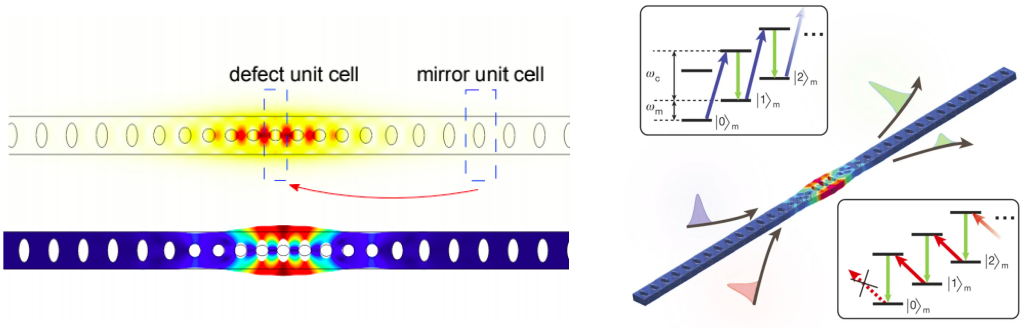

(a) *(b)*

Figure 1.1: ***Optomechanics with Photonic Crystal Cavities.*** *(a) Simulated fundamental modes of the co-localized optical (top) and mechanical (bottom) resonators in an OMC. (b) A representation of a photonic crystal cavity nanobeam as used in pulsed quantum optomechanical experiments. Insets show the level schemes for blue and red sideband operation. Images (a),(b) taken from Refs. [33, 41], respectively.*

A one-dimensional photonic crystal cavity can be patterned onto a nanobeam such that the optical defect sits on top of the fundamental mechanical breathing mode, the in-plane expansion and contraction of the beam at its midpoint. This confines the light and motion into a small volume. Under these conditions, a combination of radiation pressure back-action and the photoelastic effect can result in large interaction rates between the optical

and mechanical modes (> 1 MHz in silicon) [31]. This structure can be probed optically by pulses of light detuned from the optical cavity by the resonant frequency of the mechanical mode, depicted by the red and blue arrows in the insets of Fig. 1.1 (b). Detuning the pump laser to the red sideband of the cavity drives a 'beam-splitter'-like interaction that swaps an excitation between the photonic and phononic modes; whereas detuning to the blue sideband drives a 'two-mode squeezing'- like interaction that simultaneously creates or removes excitations in the both modes [30, 42, 43]. Early successes of silicon optomechanical nanobeams include demonstrations of laser cooling a mechanical resonator to its ground state [32], optomechanically induced transparency [44], and mechanically-mediated optical-to-optical photon wavelength conversion [45]. More recent work uses silicon OMC nanobeams to validate some elementary experiments of quantum optics including non-classical photon correlations [33], Hanbury-Brown-Twiss interferometry [46], heralded entanglement between distant mechanical resonators [47], and violation of a Bell inequality [48].

1.1.2 Tapered Optical Fibers

More than a decade of research on silicon photonic crystal cavities has produced optimized designs, efficient nanofabrication procedures, and efficient readout techniques [31, 41, 49, 50]. I will briefly dwell on the latter. Light can be coupled evanescently into these structures using single-sided tapered fibers. This is achieved by placing an optical fiber with one side adiabatically narrowed to a cone (as shown in Fig. 1.2 (a)) on top of a similarly tapered waveguide such that they overlap for a few microns. This method can transfer light with over 95% efficiency and can operate in a dilution refrigerator [51, 52].

There are many ways to make a tapered fiber; we etch the fibers by slowly pulling them out of hydrofluoric acid (HF) as shown in Fig. 1.2 (b). To make these fibers, we remove the cladding from two centimeters of one end of a SMF28 single mode optical fiber and dip it in 40% concentrated HF where it is pulled out by a motorized stage at 400 nanometers per second for 65 minutes [41, 52].

The tapered fiber coupling approach is unique because the fiber actually touches the silicon structure, unlike the other strategies which use dimpled fibers, grating couplers, or lensed fibers. In fact, silica fibers are capable of adhering to some substrates due to a van der Waals force.

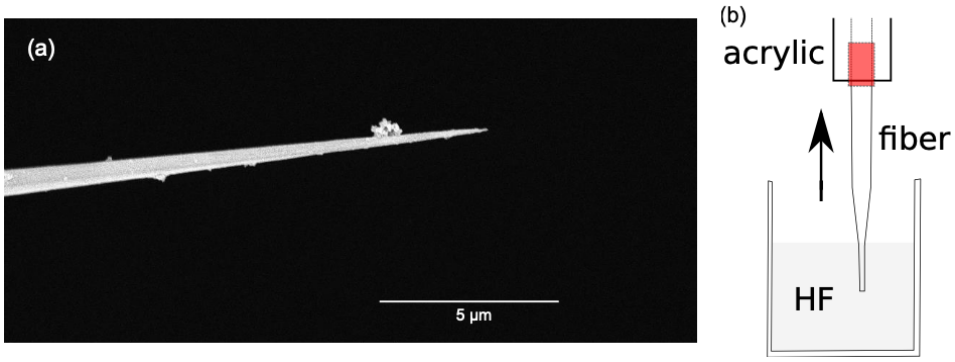

Figure 1.2: ***Pulled HF Fibers.*** *(a) A Scanning Electron Microscope image of a HF pulled tapered fiber. (b) A diagram of the fiber pulling process. Images taken from Ref. [41]*

1.1.3 Photonic Crystal Cavities, Off-Chip

Fibers stick to some materials so well that a loosely connected nanostructure can be ripped away from a chip while being measured. While this may sound like an annoyance, it also provides an opportunity for innovation. An optical fiber taper with an attached photonic crystal nanobeam, shown in Fig. 1.3, is a versatile, portable optical cavity with an extremely small optical mode volume. A series of remarkable experiments stuck such a device into a magneto-optical trap, where a silicon nitride photonic crystal cavity was coupled to cold atoms trapped in optical tweezers [53] and the atom-cavity system was used to perform quantum operations on flying optical qubits [54].

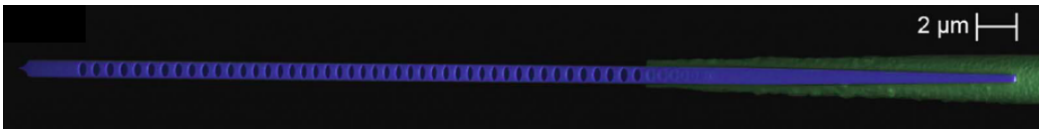

Figure 1.3: ***A silicon photonic crystal cavity on the end of a tapered fiber.*** *This structure was originally attached to a chip by a tether at the far left side. Image taken from Ref. [55]*

Recently, demonstrations of communication between two individually controlled atoms through a nanophotonic 'bus' [56] and coupling between much larger levitated silica nanoparticles and a silicon OMC nanobeam [55] have pushed this idea further. Each of these experi-

ments used a similar technique. First, suspended photonic crystal cavities were fabricated on a nanobeam with an adiabatically narrowed coupler at one end such that they are connected to the substrate by a thin (≈ 100 nm thick) tether. Then, a tapered optical fiber contacts the coupler to measure the nanophotonic device. If the device performance is satisfactory, the fiber is slowly moved back and forth to break the tether before being lifted away from the chip and into a magneto-optical trap.

1.1.4 'Pick-and-Place' Photonic Devices

We take this concept one step further by picking up nanobeams with a tapered fiber and placing them down on a piezoelectric substrate. We draw on methods developed by the silicon photonics community for hybrid material integration, where several 'pick-and-place' techniques have already been developed [57, 58]. In this subsection, we will briefly review some of these 'pick-and-place' fabrication procedures. However, our approach is unique because we can measure the reflection spectrum of the nanobeam cavities while in the process of setting them down, allowing for placement with extremely high precision.

It is not surprising that the motivation for these hybrid techniques came from the development of quantum photonics. Silicon is an ideal material for many photonic applications due to the commercial Silicon-on-Insulator (SOI) platform, high refractive index, and integrability with complementary metal–oxide–semiconductor (CMOS) electronics. However, silicon has disadvantages. Large two-photon absorption causes losses and heating. Silicon also has a centrosymmetric crystal structure and therefore displays no χ^2 nonlinearity unless strained. Furthermore, it cannot be used to deterministically generate single photons [58].

These deficits were the impetus for research into techniques where small non-silicon structures are combined with the silicon platform in order to incorporate single photon emitters and detectors, efficient non-linear components like modulators and phase shifters, and even solid-state qubits [57]. These hybrid systems can be created by growing materials epitaxially onto silicon, wafer bonding, or most simply by picking up modules of exotic materials and placing them onto a silicon photonic circuit. The latter approach is least suitable for wafer-scale integration but also offers tremendous flexibility. Unlike wafer-scale approaches, the entire silicon structure can be fabricated using a photolithography procedure in a foundry while complex structures requiring a smaller MFS (like photonic

crystal cavities) can be patterned with electron-beam lithography on a separate chip. In addition, the individual structures can be measured before integration, which is a preferable when working with devices that are fabricated with low yield such spin qubits [59] and single photon detectors [60] or emitters [61].

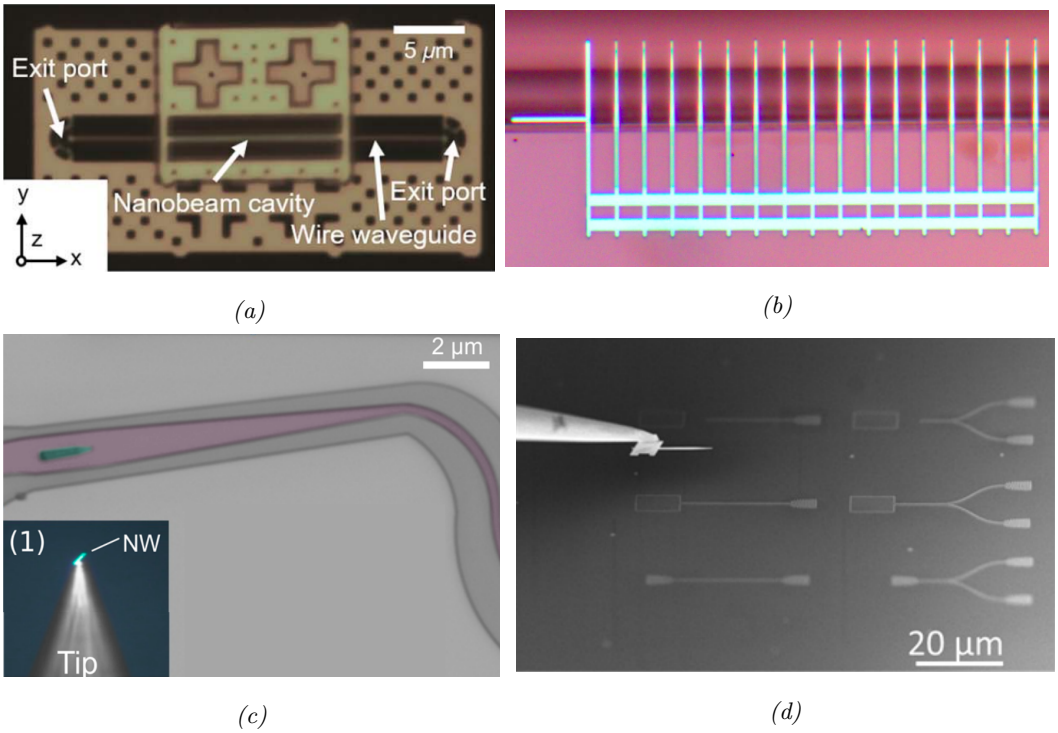

Figure 1.4: ***An Overview of 'Pick-and-Place' Photonic Devices.*** *(a) A quantum dot single photon source implanted into a nanobeam cavity (yellow) was stamped onto a silicon waveguide (orange). The crosses on top were used for alignment. (b) An array of silicon photonic crystal cavities stamped onto a rare-earth-ion substrate. Cavities were coupled from the top using a lensed fiber. (c) Superconducting nanowire single photon source (green) on a photonic waveguide (pink). Bottom left inset shows nanowire on the tip of the tungsten probe. (d) Placing a quantum dot single photon source in a photonic crystal cavity onto a silicon waveguide inside a SEM. Images taken from Refs. [61–64], respectively.*

There have been two main approaches to 'pick-and-place' fabrication: transfer printing with a polymer stamp and manipulation with a tungsten microprobe. Transfer printing

has used since the early 2000s and consists of rolling a transparent polymer stamp (usually Polydimethylsiloxane (PDMS)) over a loosely connected nanostructure to remove it from a chip, then rolling the stamp onto a different substrate to release [65]. This can be implemented with alignment markers sighted through an optical microscope to achieve impressive accuracies on the order of hundreds of nanometers in order to align a nanobeam containing quantum dots to a silicon waveguide, shown in Fig. 1.4 (a) [62]. Another experiment, shown in Fig. 1.4 (b), stamped down an array of silicon photonic crystal cavities onto an Erbium-doped crystal in order to couple individual atoms in the crystal to the cavity [63].

However, transfer printing has limitations. Optical alignment will always be diffraction limited, so precision is limited to hundreds of nanometers for visible light. In addition, the stamp exerts a force on the surrounding silicon circuit which can be problematic or even cause damage. One alternative, developed for embedding single quantum dots in vertically grown nanowires into photonic waveguides, was to pick up the minuscule structures using the finely tapered tip of a tungsten microprobe [61]. This structure, shown in Fig. 1.4 (c), acts as an integrated single photon source. The inset of this figure shows the nanowire stuck to the tip of the tungsten probe due to a van der Waals force. Larger structures can also be moved this way. In Ref. [64], quantum dots embedded in an InAs/InP photonic crystal cavity were fabricated such that they were connected by three tethers to the III-V chip. This structure was then placed into a Scanning Electron Microscope (SEM) with a focused ion beam and a manipulable microprobe. Once the microprobe made contact with the structure, the focused ion beam cut through the tethers to release the nanostructure, as shown in Fig. 1.4 (d). This procedure is extremely difficult to conduct but offers supreme alignment accuracy as the diffraction limit of a SEM is less than a nanometer.

1.2 Technique

We developed a 'pick-and-place' technique called slapping using only conventional laboratory components. This procedure is quick (experienced users can pick up and slap a device in 15 minutes) and accurate to around 100 nanometers. A fiber-based approach to construction of hybrid material platforms for transduction may seem complex and difficult to scale, but it offers some advantages over alternatives like wafer bonding or sputtering piezoelectric films. We are able to make silicon structures with excellent optomechanical

properties, but our fabrication relies on a clean dry etching process using an etcher that becomes contaminated by most materials other than silicon. Slapping allows us to fabricate these temperamental devices and transfer them to a piezoelectric electromechanical device.

1.2.1 Slapping Procedure

Our procedure consists of the following three steps:

1) Fabrication: First, suspended nanostructures are fabricated to be loosely connected to their substrate by a thin tether on a "donor chip," as displayed in Fig. 1.5 (a). The donor chip can be constructed from different materials, each of which has a different fabrication flow. This section aims to give an overview of design considerations rather than a recipe. Fabrication procedures for lithium niobate and silicon are shared in detail in Sections 2.3.2 and 3.2.2, respectively. Note that the tethered structures are fragile when undercut, so we recommend using dry or vapor etching processes (instead of wet ones) for release.

The donor chip typically contains a large number of small structures written with small features (in our case, photonic crystal cavities). In order to slap them, we connected these structures to the substrate with a single thin strip of material called a tether. We also etch away a large area around the structure. We found that slapping worked best when there was at least 10 microns of empty space to either side of the structure and 100 microns of empty space adjacent to the edge of the chip so that the tapered fiber can approach the suspended structure without touching the chip. After etching, a large-radius ($> 5\mu m$) undercut is performed, leaving the structure suspended.

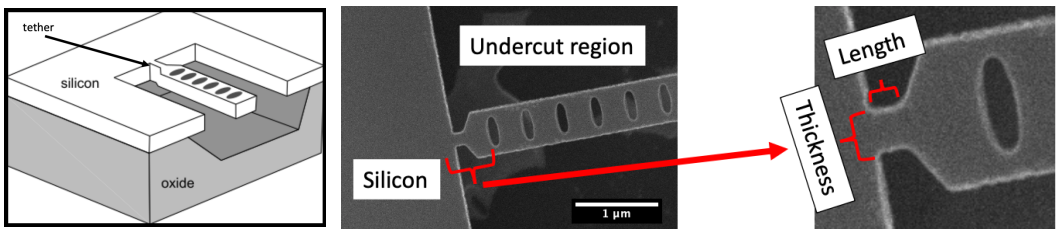

(a) *(b)*

Figure 1.5: ***Suspended, Tethered Nanostructures for Slapping.*** *(a) A diagram of a photonic crystal cavity on a donor chip. (b) Birds-Eye SEM image of a nanostructure connected to the donor chip. Inset shows the tethered region more detail.*

The tether is the critical part of this design: if the tether is too weak, the structures will collapse after they are undercut, but if it is too strong, the structures will not break away from the chip during slapping. A tethered photonic crystal nanobeam is shown in Fig. 1.5 (b) in which we label the two dimensions of the tether, the thickness and width. In our experience, good tether parameters varied somewhat for different structures and materials, and thus require a cycle of trial-and-error to find. We observed that structures are more sensitive to changes in the tether thickness than the length. Generally, we used thicknesses between 80 and 100 nanometers and lengths between 50 and 150 nanometers.

2) Pick Up: Next a tapered fiber is brought close to the sample and tears away the suspended nanostructure, as shown in Fig. 1.6 (a). In order to achieve this we constructed a 'slapping setup' consisting of a motorized three-axis stage (Mechonics MX35) mounted on rotation and tip/tilt stages, a microscope and camera, and a single-axis motorized stage (Thorlabs MTS50-Z8) with an attached tapered optical fiber (SMC28 fiber, etched in HF as described in Section 1.1.2). The donor chip is placed on the three-axis stage and brought into the camera's focus. Then the tapered fiber is mounted 1-2 degrees from horizontal with respect to the chip such that the tapered end will touch the chip before the fiber. The fiber is connected to the second motorized stage such it can be lifted up and down from the surface of the donor chip. Then, the fiber is slowly lowered until it is almost in focus. It is helpful to touch down the fiber onto the surface of the chip at a location away from the devices to get an understanding of the nanostructure height in calibrated coordinates.

At this point, everything is prepared to pick up the structure. This can be broken down into in five stages, which are shown in Figs. 1.6 (b-f) with a lithium niobate nanobeam (not a photonic crystal, but with roughly the same dimensions as one). Once the fiber and nanostructure are both roughly in focus, rotate the chip such that long axes of the fiber and the devices are aligned such that the tip of the fiber is pointed toward the end of the nanostructure (the farthest point from where it is tethered). In photonic crystal devices, this end is a coupler. The view from the camera should look like Fig. 1.6 (b). Then, the fiber is brought to hover over the end of nanostructure and slowly lowered until it sticks, as seen in Fig. 1.6 (c). The experimenter will know when the fiber is touching something because the color of the tip of changes dramatically. It is best to touch the structure as little as possible because the more overlap that the structure has with the fiber, the more difficult it is to remove later on. Once the fiber is stuck, the goal is to break the tether

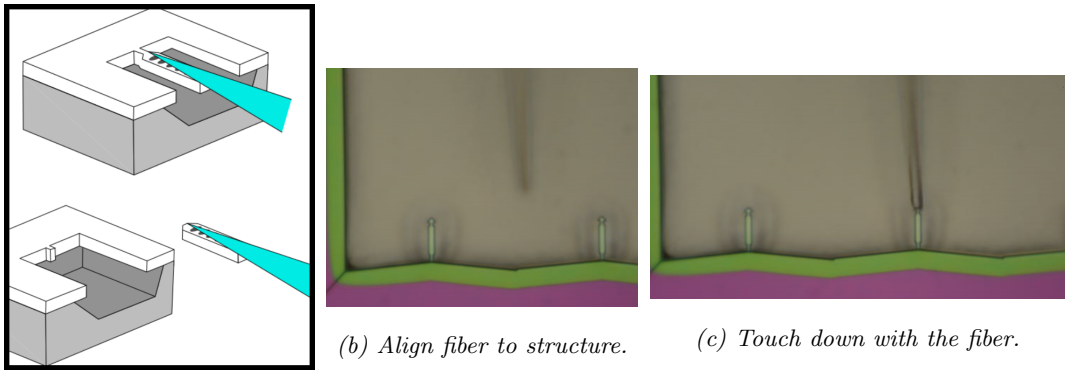

(a)

(b) Align fiber to structure.

(c) Touch down with the fiber.

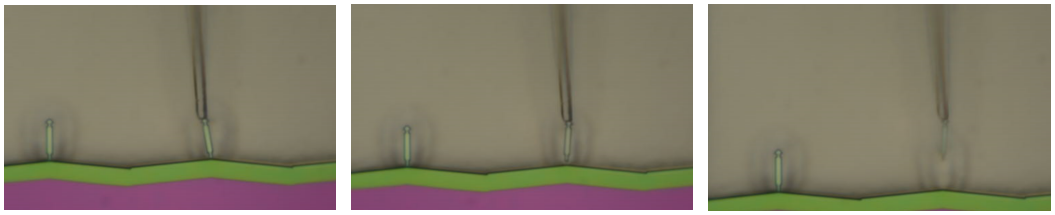

(d) Wiggle the structure.

(e) Break the tether.

(f) Pull back and lift away.

Figure 1.6: ***Picking Up Nanostructures with an Optical Fiber.*** *(a) Diagram of an optical fiber adhering to the nanostructure and ripping it away. Sub-figures (b-f) are optical images of the five stages of pickup. In these pictures, fiber is clear, suspended lithium niobate is green, non-suspended lithium niobate is pink, and the undercut region is gray.*

and move the structure away from the chip. We accomplish this by moving the stage left and right one or two microns at a time, wiggling the structure in order to strain and break the tether. The agitation shown in Fig. 1.6 (d) has successfully broken the tether in Fig. 1.6 (e). Finally, the structure stuck to the fiber can be pulled away from the substrate and lifted away from the chip (Fig. 1.6 (f)).

3) Slap Down: The fiber is raised from the donor chip and lowered onto a "device chip," where the nanostructure is released as shown in Fig. 1.7 (a). If the pick up went correctly, this can be very simple. First, the fiber is raised to a safe distance (> 1 millimeter) and the donor chip is removed from the motorized stage and replaced by the device chip. At this point we use the tip/tilt functionality of our positioning stack to increase the angle of the tapered fiber with respect to the chip by a few degrees. This makes sure that the

nanostructure contacts the surface of the device chip before the fiber. Then the fiber is lowered until the nanostructure is visible. We use the linear and rotary stages to align the angle and the position of the nanostructure with the desired location on the device chip.

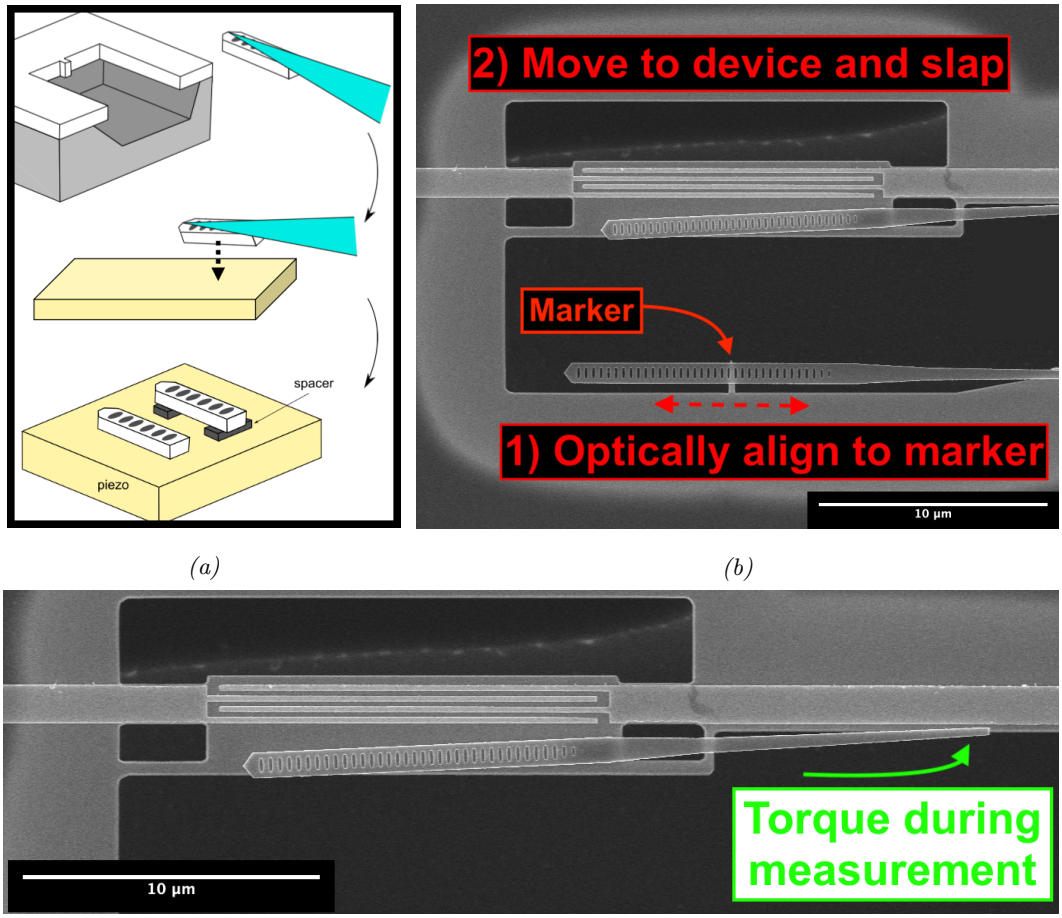

(a) *(b)*

(c)

Figure 1.7: ***Slapping Down Nanostructures.*** *(a) Diagram of the structure being lifted away from the donor chip, aligned to the device chip, and placed down. (b) This SEM image illustrates our alignment procedure. Nanobeams are first positioned above the marker at the bottom of the device to find the center of the photonic crystal cavity. Then they are moved vertically to their desired position on the device. The two nanobeams shown here are both real - the bottom one was accidentally slapped during alignment. (c) The nanobeam in this SEM image was initially positioned correctly but the alignment was ruined during measurement.*

Then, the fiber is lowered slowly (about 1 micron at a time) until the device makes contact with the substrate. The device should stick to the substrate better than it does to the tip of the fiber. Sometimes it seems to fall off the fiber and into place, while other times the operator needs to pull the fiber away by slowly dragging away from the structure.

While the procedure outlined above is sufficient for some applications, its precision ultimately depends on the quality of optical alignment which is bounded by the diffraction limit. One way to place devices more precisely is to repeat this procedure inside of a SEM, as demonstrated in Ref. [64]. However, one of the major benefits of slapping is its simplicity, and micro-manipulation inside of an SEM is quite complex (and expensive!). We developed an alternative method for optimal alignment of photonic crystal cavities which makes use of reflection measurements through the tapered fiber during the slapping procedure. We send input light from a tunable laser into the tapered fiber and measure the reflected output on a photodiode. If you pick up a photonic crystal cavity such that the coupler overlaps with the tapered fiber (seen in Fig. 1.3), you can measure the reflection spectrum of the cavity. This spectrum consists of Lorentzian dips corresponding to the cavity modes, and the linewidths of the dips depend on the effective refractive index of the optical mode. The linewidths are significantly larger when the cavity is hovering over a chip than when it is surrounded by air due to the drop in effective refractive index contrast.

Because the optical mode in the nanobeam is highly localized, we can use this effect to align the cavity. We do so by patterning a thin marker in the otherwise empty suspended region of the device. By hovering over this marker and moving the fiber back and forth as indicated by the dotted red arrow in Fig. 1.7 (b), we can find the region where the linewidth of the fundamental optical mode is largest and confidently position our optical cavity in one direction. Then, we simply move the structure to its desired location on the device and slap it down. We used the same trick, concurrent measurement of the reflection spectrum, to understand when we were exactly lined up with the edge of the device, which helps calibrate our position in the perpendicular direction.

However, it is easy to see that the nanobeam in Fig. 1.7 (b) is not aligned. This is due to an issue with our experimental design: our measurement requires contact between the nanobeam and a tapered fiber. Small movements of the fiber or the chip can reposition or even unslap the nanobeam. Fig. 1.7 (c) shows a magnified image of the same device. One can see how the device was originally assembled correctly, but movement of the fiber during

measurement torqued the nanobeam and crashed the end into the side of the lithium niobate resonator, which ruined the positioning. We have learned that we should use a contact-free measurement technique in future experiments, as it is better to not touch nanobeams once they have been slapped. This issue will be revisited in Chapter 3.

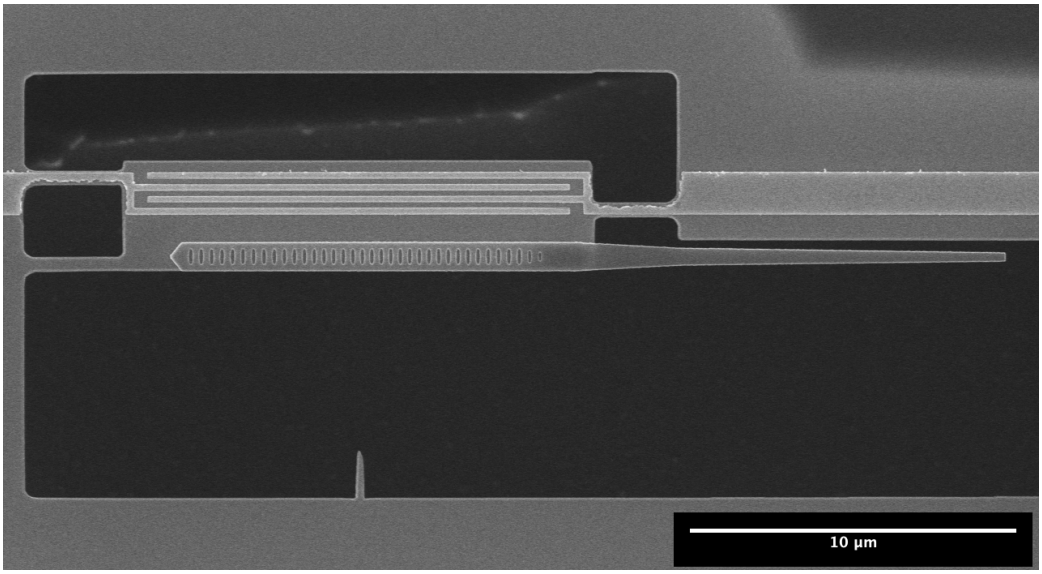

Figure 1.8: ***Slapped Silicon Nanobeam.*** *A silicon photonic crystal nanobeam slapped onto a lithium niobate thin film resonator. The marker at the bottom was used to align the cavity to the middle of the mechanical resonator during slapping.*

In this chapter, we have successfully developed a method for slapping silicon photonic crystal cavities nanobeams. The precision of this method is still limited by the step size of the minimum step of the motorized stage (ours was 100 nm) as well as the angular alignment. We adjusted the angle by eye and found that we could consistently slap with less than 2 degrees of misalignment. This was sufficient for our purposes and allowed us to place nanobeams on our substrate very accurately, such as the one shown in Fig. 1.8. In Chapter 3, we demonstrate piezo-optomechanical transduction with similar devices.

1.2.2 Considerations and Future Improvements

A few notes from the author to those who consider using this technique in the future:

- Occasionally the structure can make partial contact with the surface, indicated by a

diffraction pattern visible in the device. Once the device is off of the fiber, the fiber can be used to 'press' the structure smoothly onto the surface. If attempted carefully using small movements of the fiber, this can be done without moving the structure. Alternatively, one can use larger movements to slide the structure around on the chip. This can be useful, as many small errors in positioning can be corrected after slapping.

- We successfully slapped structures made of silicon, silicon nitride, gallium arsenide, and lithium niobate during this project. However, that does not mean that slapping works for all materials. Slapping requires the device to stick to the substrate of the device chip better than it sticks to the optical fiber. The 'stickiness' of a material depends on many factors, and it may take some investigation to discover why a material does or does not seem sticky to slapped structures. We are confident that surface roughness is important to consider, as we were able to slap our structures onto smooth substrates like thermally-grown silicon oxide and MOCVD-grown silicon nitride while the same structures would not stick to rough substrates like PECVD-grown silicon oxide or LPCVD silicon nitride.

- One of our earlier designs, shown in Fig. 1.9 (a), consisted of a photonic crystal cavity attached to two pads on one side and a coupling waveguide on the other. We had no problem removing these devices from the donor chip, however we found that they tend to slide around on the tip of the fiber because their weight is not distributed equally about the fiber's point of contact. Therefore, we recommend attempting to slap with symmetrical structures.

- Over the course of this research we experimented with structures of various geometries. Early on, we wanted to suspend a nanobeam over a piezoelectric surface acoustic wave resonator by slapping down large silicon blocks before slapping our nanobeam. The largest blocks we were able to pick up without modifying our technique were 6×8 microns, shown in Fig. 1.9 (b). This gives us a upper bound on the largest structures that we can slap using the technique laid out in this chapter.

- While we eventually moved away from the idea of slapping silicon pads, we were able to place a photonic crystal cavity nanobeam onto sputtered pads of molybdenum rhenium (MoRe), shown in Fig. 1.9 (c). We measured that this nanobeam was suspended ≈ 50 nanometers above the lithium niobate substrate.

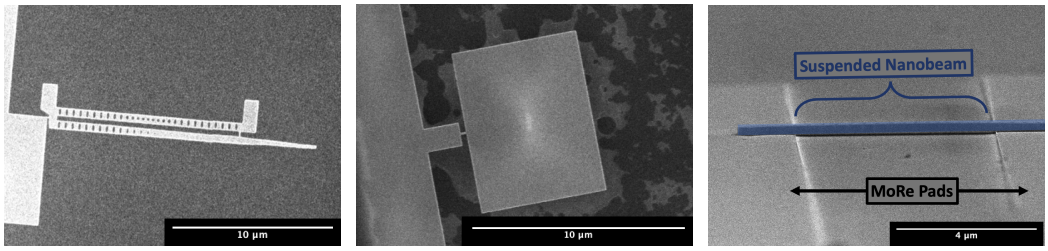

(a) *(b)* *(c)*

Figure 1.9: ***Pushing the Limits of Slapping.*** *(a) A silicon nanobeam with a reflector tethered to a donor chip. When we picked this structure up by the tapered waveguide, it tended to roll around the tip of the fiber. (b) A* 6×8 *µm silicon block on a donor chip. While there is a bit of silicon oxide left on the bottom of the chip at the center due to a short release, the block is still suspended. (c) A silicon nanobeam (false color, blue) suspended on sputtered MoRe pads over a lithium niobate substrate.*

- When the author first attempted this technique, he was afraid of breaking a tapered fiber. However, after much experience smashing and clobbering a few tapered fibers, he has reached the conclusion that they are really quite robust. When making movements of fewer than 10 microns the fiber has a greater propensity to bend than to break. If a piece of the tapered fiber tip does break, that is not the end of the world - broken tips can stick to structures just as well as clean ones. In fact, we often re-used 'broken' tapered fibers from our lab's optical characterization experiments for slapping.

- Finally, there are many extensions of this technique. We want to mention one possibility that reverses the order of our method: slapping nanostructures onto an empty chip *before* patterning the device. By using an alignment procedure similar to that described in Ref. [66], we could use on-chip markers to calibrate the position of a slapped nanobeam and pattern a piezoelectric resonator around . This requires the nanostructure to survive the fabrication. We tested this by slapping some nanobeams and then spinning, baking, patterning, and etching a structure on the same chip, and saw that the structures survived. No further progress was made in this investigation, but continued research in this direction would be very interesting to the author.

Chapter 2

Thin Film $LiNbO_3$ Bulk Acoustic Resonators for Transduction

Our goal is to build a piezo-optomechanical GHz-THz conversion device, which in its final form will consist of a piezoelectric mechanical oscillator coupled to both an optical and a microwave resonator. We chose to combine silicon photonic crystal cavities, a relatively robust and well-understood optomechanical platform [31, 47, 67], with a piezoelectric acoustic resonator. Our hybrid assembly technique gives us complete freedom over the design of this resonator. In this chapter, we determine which material, geometry, and mechanical mode are optimal for the task of wavelength conversion. Section 2.1 examines in depth which properties lithium niobate make a good material for electromechanical conversion and how the material compares to other piezoelectrics. In Section 2.2 we discuss how we engineered our acoustic resonators and in Section 2.3 our fabrication procedure is described and discussed. Finally, in Section 2.4, we present and analyze measurements of our resonators.

2.1 Lithium Niobate

One of the critical design decisions for a piezo-optomechanical transducer is the choice of piezoelectric material. Four primary candidates have emerged: aluminum nitride (AlN) [18, 25, 39, 68, 69], gallium arsenide (GaAs) [24, 38], gallium phosphide (GaP) [36, 37], and

lithium niobate (LN) [22, 23]. The challenge of piezo-optomechanical transduction can be broken down into the subproblems of efficient optomechanical and electromechanical transduction. An ideal material for this task would have a large refractive index, low two-photon absorption, and demonstrate strong piezoelectricity. However, no material has completely favorable properties. Therefore, monolithic fabrication strategies require a choice between piezoelectrics with better optomechanical and worse electromechanical properties (i.e. GaAs,GaP) or vice versa (i.e. LN, AlN). The strength of our hybrid fabrication approach is that we are not faced with such a compromise - we are free to choose the best materials for facilitating both optomechanical and electromechanical interactions.

We chose to use lithium niobate ($LiNbO_3$), a colorless, non-naturally occurring dielectric material which is known for its large piezoelectric, electro-optic, photo-elastic coefficients [70]. An important figure-of-merit for an electromechanical device is the effective coupling coefficient, k^2, defined as the mechanical (electrical) energy stored per electrical (mechanical) energy applied.[1] Lithium niobate supports bulk acoustic modes with the largest k^2 of any material suitable for efficient electromechanical conversion. This value can be as high as 30% in LN [71], compared to $k^2_{max} = 7\%$ in AlN, .4% in GaAs, and .2% in GaP [72].

The demonstration of lithium niobate high-overtone bulk acoustic resonators (HBARs) with extremely large frequency-quality factor products ($\approx 10^{13}$) indicate that intrinsic acoustic losses will not limit our investigation [73]. Furthermore, multiple demonstrations of qubits coupled to thin film lithium niobate resonators prove that this platform is compatible with emerging superconducting qubit technologies [28, 29]. This is important because our device must interface with a qubit to ultimately have useful applications in quantum information.

Relevant Piezoelectricity Properties

When lithium niobate was first synthesized at Bell Laboratories in the 1940s, researchers remarked that it has a high melting point (1255° C) and Curie Temperature (1142° C) and exhibits ferroelectricity [74]. By 1965, the development of a process to grow single crystals using the Czochralski technique allowed for the mass production of large and low-defect crystals at any growth orientation [70, 75]. Below the Curie temperature the trigonal

[1] Some literature uses the notation k^2_{eff} or k^2_t for the effective coupling coefficient.

crystal enters a ferroelectric phase, where lithium and niobium atoms shift away from the central locations of the planes, giving lithium niobate its non-centrosymmetric structure which results in piezoelectric properties at all temperatures relevant to this work [70, 75]. Single-crystal lithium niobate has been in commercial use since the 1960s; at first used for analog acoustic signal processing in acoustic transducers, filters, and delay lines and later for integrated optics in electro-optic modulators and dielectric waveguides [76].

Piezoelectric solids have a linear relationship between the mechanical deformation of the solid and electric field. This can be expressed as a relation between the stress and polarization of the solid, known as the piezoelectric effect

$$P_i = \sum_{j,k} d_{ijk}\sigma_{jk} \tag{2.1}$$

where P_i is the induced polarization, σ_{jk} is the second-order stress tensor, d_{ijk} is the piezoelectric tensor, and $i, j, k = x, y, z$. The piezoelectric tensor d_{ijk} also describes the relation between strain and electric field, known as the converse piezoelectric effect

$$S_{jk} = \sum_{i} d_{ijk}E_i \tag{2.2}$$

Due to crystal symmetries and thermodynamic arguments, the piezoelectric tensor can be reduced to a 3 x 6 matrix described by four independent numbers [70]. The convention is to write the jk subscripts corresponding to the components of the stress tensor as a single subscript in the reduced matrix, specifically $jk = 11, 22, 33 \implies 1, 2, 3$, $jk = 23, 32 \implies 4$, $jk = 13, 31 \implies 5$, and $jk = 21, 12 \implies 6$. Using this notation, we represent the piezoelectric tensor of lithium niobate as

$$d_{ijk} = \begin{bmatrix} 0 & 0 & 0 & 0 & d_{15} & -2d_{22} \\ -d_{22} & d_{22} & 0 & d_{15} & 0 & 0 \\ d_{31} & d_{31} & d_{33} & 0 & 0 & 0 \end{bmatrix} \tag{2.3}$$

Piezoelectric Strain Coefficients [10^{-12} C/N]

d_{15}	d_{22}	d_{31}	d_{33}
69.2	20.8	-0.85	6.0

In order to understand this matrix, it is useful to use the think about three different classifications of the piezoelectric effect, illustrated in Fig. 2.1 [77]. The first is the longitudinal effect, represented by the elements $d_{ii} = d_{11}, d_{22}, d_{33}$, where an applied electric field and the induced strain occur in the same direction. The second is the transverse effect, represented by $d_{ij}, j = 1, 2, 3, i \neq j$, where an electric field applied along one direction causes an extension perpendicular to the applied field. Finally, there is the shear effect, represented by $d_{ij}, j = 4, 5, 6$, where applied electric field leads to shearing stress in the crystal. We can conclude from Eq. 2.3 that the piezoelectric effect couples applied electric field most strongly to mechanical modes actuated by shear stress. The next largest coupling is to modes which produce longitudinal stress, and the weakest coupling is to transverse-type modes.

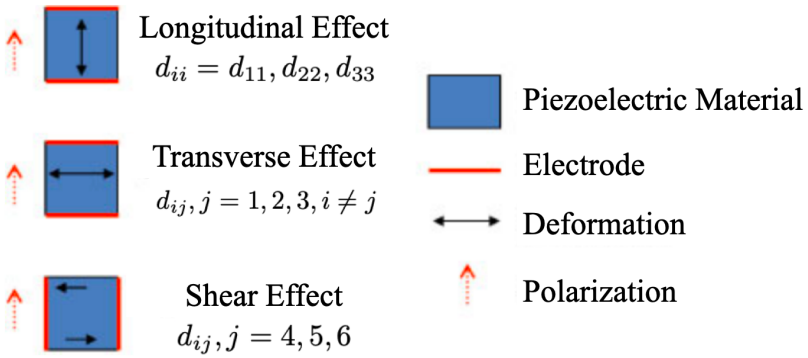

Figure 2.1: ***Piezoelectric Modes.*** *An applied electric field can generate three different strain responses, each related to a certain group of piezoelectric strain coefficients. Image is taken from Ref. [77]*

By comparing the magnitude of lithium niobate's piezoelectric strain coefficients to those of other materials of interest, we can immediately see its advantage. Its largest coefficient, d_{15}, is 69.2 pC/N while the largest coefficient in aluminum nitride is 5.0 [78] and in gallium arsenide is 2.69 [79]. It should be noted that the piezoelectric tensor does not completely characterize this deformation of a piezoelectric material due to electric field as it does not account for elastic and dielectric properties. A full understanding of the acoustic response therefore requires exploring the elastic stiffness and compliance matrices (for lithium niobate, these can be found in Ref. [75]). However, lithium niobate's large piezoelectric coefficients contribute to its large electromechanical coupling compared to other materials currently

used for piezo-optomechanical transduction.

Crystal Orientation

Many different cuts of lithium niobate are commercially available. Ref. [75] notes that the Z-cut and 36° Y-cut are usually preferred when taking advantage of the longitudinal piezoelectric effect, while the X-cut and 139° Y-cut are most often used for shear-mode devices. We chose to purchase a X-cut thin-film LNOS (lithium niobate on silicon) wafer from NGK Insulators, LTD with a 330 nm film of $LiNbO_3$ on a 500 μm silicon substrate. The crystal is doped with 5mol% MgO to lower optical absorption at telecom wavelengths [80]. This cut was selected because it the most flexible, giving us the option to use longitudinal, transverse, or shear-type modes depending on our direction of propagation. It was also the choice for the thin film bulk acoustic resonator devices that inspired our own designs [81].

2.2 Designing a Resonator

Our competent understanding of the components of lithium niobate's piezoelectric coupling matrix allows us to design a piezoelectric resonator. These resonators can come in many shapes and sizes and each resonator geometry supports many modes, so there are a lot of choices to be made. In this section we identify the appropriate design criteria and justify our choice of resonator geometry and mode.

2.2.1 Resonator Selection

We came up with some design guidelines for our mechanical resonator. Firstly, we want our resonator to support modes with both large Q factor and large k^2 in order to have the highest possible piezoelectric coupling and lowest losses. The resonator should also be capable of interfacing with a slapped photonic crystal nanobeam. Our plan is to integrate this mechanical resonator with a photonic crystal cavity, so the geometry of the resonator should allow for an optical coupler and waveguide to be accessible during measurement. Finally, we aim to keep fabrication as simple as possible.

There is a diverse family of acoustic resonators that have been richly explored during

decades of use as Radio Frequency (RF) oscillators and filters, but these criteria narrow down our options considerably. We have already chosen lithium niobate as our piezoelectric material to attempt to find a mode with high k^2 and Q. We considered two options for making acoustic resonators on lithium niobate: Surface Acoustic Wave (SAW) and thin film Bulk Acoustic Wave (BAW) resonators[2], shown in Fig. 2.2. SAW resonators are a good option as they are large, easy to excite, and are capable of being strongly coupled to transmon qubits [28] and integrated with several other hybrid quantum systems [72]. Thin film BAW resonators in lithium niobate are also an active area of research as a next-generation alternative to aluminum nitride contour-mode resonators (CMRs) in RF filters [82]. These devices consist of a suspended slab of thin film of lithium niobate, anchored by thin tethers, with electrodes patterned on top to actuate bulk acoustic modes in the slab. More recently this platform was also successfully integrated with superconducting microwave circuits [83]. In addition, both SAW and thin film BAW devices can be fabricated with resonances varying between 1-10 GHz.

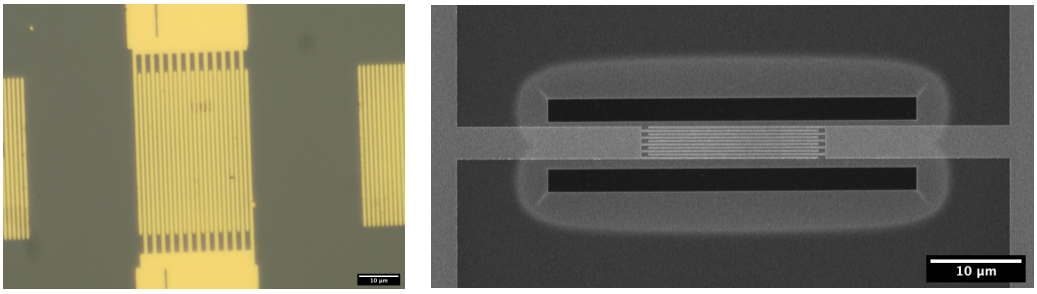

(a) *(b)*

Figure 2.2: ***Acoustic Resonators.*** *(a) Optical image of a SAW resonator. The gold electrodes in the middle launch SAWs into the bulk lithium niobate which bounce off of the gold Bragg Reflectors on either side. (b) SEM image of a thin film BAW resonator. The gold electrodes in the middle excite BAWs in the suspended lithium niobate film.*

These waves are all excited by lateral electric fields and thus encourage the use of Interdigital Transducers (IDTs), a practical and adjustable electrode configuration. The spacing between fingers of the IDT, or pitch, determines which modes are excited in the piezoelectric film underneath. The bandwidth of excited modes is inversely proportional to the number

[2]Some literature uses Film Bulk Acoustic Resonator (FBAR) instead of thin film BAW resonator

of finger pairs of the IDT [84]. Deeper analysis of optimizing the coupling to these modes to IDTs is conducted in [85].

We opted to investigate a thin film BAW design for two main reasons. Firstly, the mode volume and effective mass of excitations in thin film resonators are intuitively much smaller than that of excitations in a SAW resonator, as there is less mass to displace in the former. This will help our device achieve maximum coupling to our (comparatively much smaller) optical cavity. Secondly, thin film lithium niobate resonators offer higher maximum potential electromechanical coupling (around 30% compared to 10% in SAW devices [71]). Also, because the acoustic confinement of thin film BAW devices is superior to inevitably leaky SAW devices [86], it is likely that the maximum quality factor of thin film BAW resonator modes is higher than SAW resonator modes.

2.2.2 Mode Selection

Next we will discuss which of the bulk modes of a thin film resonator are optimal for microwave to optical transduction. As discussed, we want to find a mode with large electromechanical coupling, which is determined by the geometry as well as the electrode configuration. We also want our mode to have low loss rates compared to its frequency, which depends on the internal loss mechanisms of the device. In the case of a thin film BAW resonator, the biggest preventable losses are likely to come from sub-optimal tether placement and scattering off of uneven sidewalls.

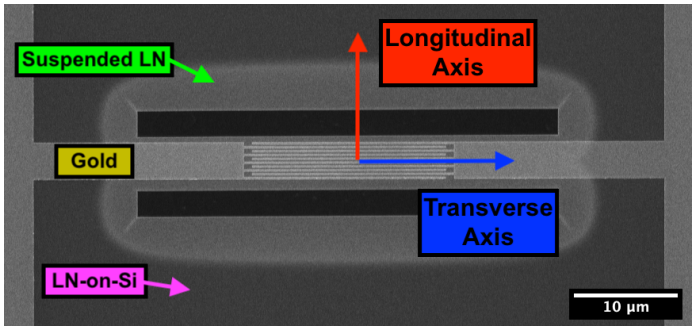

Figure 2.3: ***Device Geometry.*** *SEM image with the materials and axes labeled. The transverse axis runs parallel to the electrodes, while the longitudinal axis cuts across them.*

Our strategy is to understand the modes that will be present in our resonator, then

select the one we want to use and finally find an electrode configuration that maximizes coupling to the desired mode. We will focus on three solutions to the wave equation in the free isotropic plate, as discussed in [87]: The zeroth-order symmetric (S0) and antisymmetric (A0) lamb waves and zeroth-order shear horizontal (SH0) waves. Each solution has a transverse and longitudinal component, and the use of 'zeroth-order' here refers to solutions with the lowest transverse mode order. There are many A0, S0, and SH0 solutions in a given acoustic resonator, each defined by a different longitudinal mode order. The transverse and longitudinal axes are defined for each device as shown in Fig. 2.3. We made a finite element simulation using the piezoelectricity package in COMSOL Multiphysics 5.4 in order to analyze each of these modes.

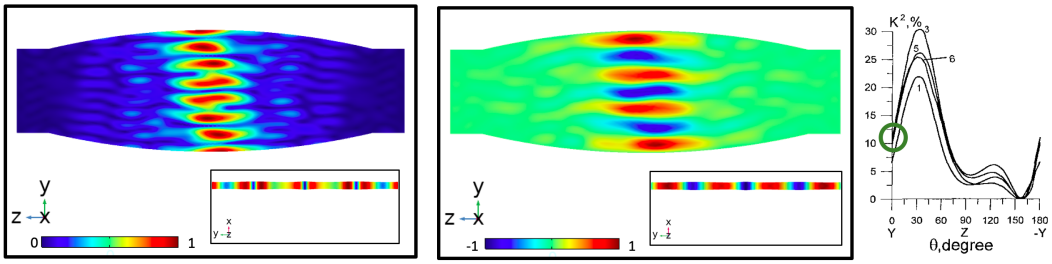

(a) *(b)* *(c)*

Figure 2.4: ***The Symmetric Lamb Wave, S0.*** *In (a) and (b), the simulated displacement profile and the largest component of the strain, ϵ_{yy}, of the S0 mode at 3.21 GHz are plotted respectively, in arbitrary units. A birds-eye view is used in the main image, while a longitudinal cross-section is shown in the inset. Crystal axes are also included. In (c), the angular dependence of the intrinsic electromechanical coupling (K^2) of X-cut lithium niobate is shown, taken from [88]. Different lines indicate different thicknesses of the film. The parameter regime of device simulated in (a,b) is circled.*

The motion of the symmetric lamb wave mode, S0, is longitudinal in-plane expansion and contraction of the film under pairs of electrodes in the same direction as the field. A simulation of the mode shape is shown in Fig. 2.4 (a). In X-cut lithium niobate oriented such that the y axis of the crystal lies along the mode's direction of propagation, this mode is piezoelectrically coupled by the longitudinal component d_{22} (see Eq. 2.3), the second largest piezoelectric strain coefficient. Therefore, the resulting strain field is dominated by ϵ_{yy}, the component in the same direction, which is plotted in Fig. 2.4 (b). This mode displays a large

electromechanical coupling which varies as a function of the propagation direction, as shown in Fig. 2.4 (c) [88]. One should note that this graph plots the value of K^2, the intrinsic electromechanical coupling. This value sets the maximum total electromechanical coupling: when the electrodes are in an optimal configuration, the electromechanical coupling is given by the equation $k^2 = \frac{K^2}{1+K^2}$ [82]. The maximum coupling ($K^2 > 30\%$) occurs at an orientation of 30 degrees from the y axis. Even without modifying our device to accommodate an optimal propagation direction, the coupling in the y direction of propagation is 10%, as high as any surface acoustic mode.

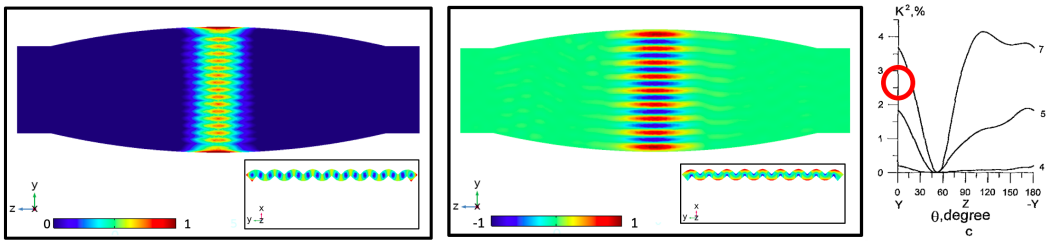

(a) *(b)* *(c)*

Figure 2.5: ***The Asymmetric Lamb Wave, A0.*** *In (a) and (b), the simulated displacement profile and the largest component of the strain, ϵ_{yy}, of the mode at 3.34 GHz are plotted respectively, in arbitrary units. A birds-eye view is used in the main image, while a longitudinal cross-section is shown in the inset. Crystal axes are also included. In (c), the angular dependence of the intrinsic electromechanical coupling (K^2) of X-cut lithium niobate is shown, taken from [88]. The parameter regime of device simulated in (a,b) is circled.*

The motion of the asymmetric lamb wave mode, A0, is also longitudinal, but unlike S0 the displacement occurs out of plane. This mode shape is plotted in Fig. 2.5 (a). Similarly to S0, the strain field of A0 is primarily coupled to the electric field by d_{22} (the resulting dominant strain component, ϵ_{yy}, is plotted in Fig. 2.5 (b)). However, unlike S0 the strain maximum and minimums occur opposite from each other on the surfaces of the film directly under each electrode. The result is that A0 has a significantly lower k^2 in X-cut lithium niobate as shown in Fig. 2.5 (c), which is why it is considered to be undesirable in commercial devices.

The phase velocity of S0 modes is approximately double that of A0 modes [88]. However, an IDT excites one wavelength of an A0 mode between adjacent fingers, while a S0 wave is

formed between adjacent finger pairs. Therefore, the same IDT will actuate both S0 and A0 waves but S0 waves will have twice the wavelength as A0 waves. $v = \lambda f$ so A0 and S0 modes are usually found in similar frequency regimes.

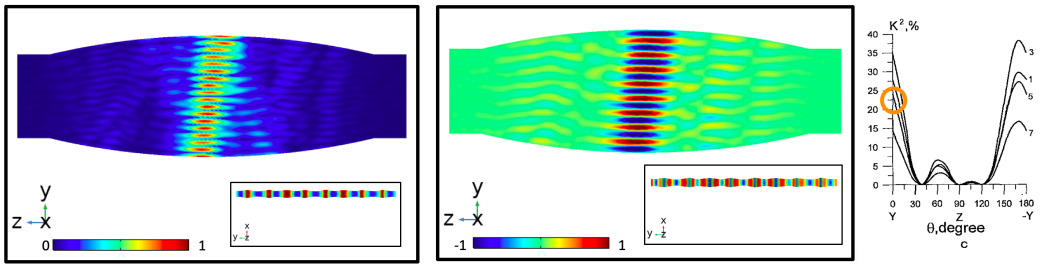

(a) *(b)* *(c)*

Figure 2.6: ***The Shear Horizontal Wave, SH0.*** *In (a) and (b), the simulated displacement profile and the largest component of the strain, ϵ_{yz}, of the mode at 5.05 GHz are plotted respectively, in arbitrary units. A birds-eye view is used in the main image, while a longitudinal cross-section is shown in the inset. Crystal axes are also included. In (c), the angular dependence of the intrinsic electromechanical coupling (K^2) of X-cut lithium niobate is shown, taken from [88]. The parameter regime of device simulated in (a,b) is circled.*

Finally, we will discuss the horizontally polarized shear mode, SH0. Though this mode is excited by the exact same IDT structure as S0 and A0, the motion of the mode (displayed in Fig. 2.6 (a)) consists of transverse expansion and contraction (instead of longitudinal). This mode is coupled to the electric field by the shear component d_{24}. Therefore, the shear strain ϵ_{yz}, plotted in Fig. 2.6 (b), is the dominant strain component. We can determine from Eq. 2.3 that $d_{24} = d_{15} \approx 3 \cdot d_{22}$, so we can assume that SH0 is easier to excite than A0 and S0. Indeed, we maximum strain in a SH0 mode (3.67×10^{-3}) is about an order of magnitude larger than it is in S0 (8.11×10^{-4}) and A0 (3.29×10^{-4}) modes. The intrinsic electromechanical coupling $K^2 = 22\%$ of the SH0 mode, plotted in Fig. 2.6 (c), is the largest of all zeroth-order bulk acoustic waves for this geometry. In addition, the phase velocity of SH0 modes is much larger than that of A0 modes. As a result SH0 modes occur at higher frequencies than A0 and S0 modes of the same order [88].

Now that we have produced a resonator design and studied its acoustic mode structure, we will fabricate and test several generations of devices in order to understand which mode is most suitable for use in a microwave to optical transduction device.

2.3 Fabrication

2.3.1 Comments on Etching Lithium Niobate

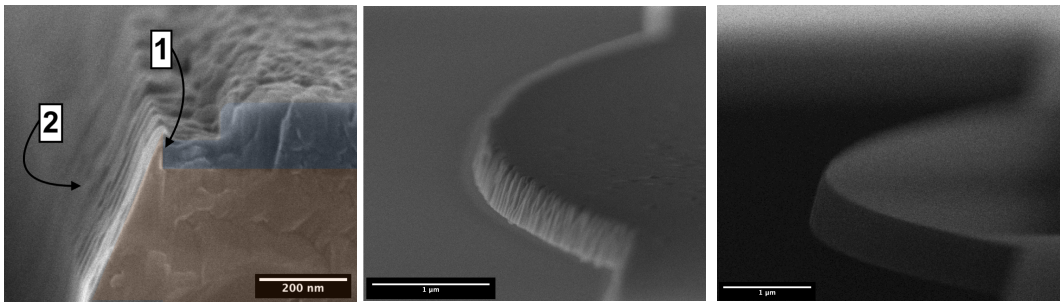

(a) *(b)* *(c)*

Figure 2.7: ***Developing an Effective Lithium Niobate Etch.*** *(a) SEM image of lithium niobate after ion milling, with the profile in false color. LN is orange and the remaining resist is blue. After milling through the LN, angular features about 45 nm wide and 60 nm tall are redeposited above the LN layer of our sample, indicated by marker 1. Marker 2 points to the resulting rough sidewalls. (b) A curved structure in a suspended thin film of LN shows the same issues. (c) The same device after RCA-1 cleaning. The sidewalls appear smooth and redeposited features are not present. The sidewall angle is measured to be* $75°$.

Despite being a widely used material across multiple industries for decades, nanofabrication using lithium niobate is considered difficult. There is no known chemical wet or dry etch for lithium niobate that produces desirable devices with acceptable sidewalls and low surface roughness without unwanted contamination from byproducts. Fluorine-based reactive ion etching (RIE) nearly always grows crystalline films of rough and difficult to remove lithium fluoride (LiF) on the surface of the etched lithium niobate [89]. Chlorine-based RIE processes which utilize a hard mask (often Chromium) have been developed, but even this complicated process results in unacceptably rough and sidewalls which cause large losses in acoustic resonators and makes fabrication less reproducible [71,81]. The problem of etching lithium niobate is considered so difficult that most commercial processes for optical devices do not even attempt it; they resort to making hybrid waveguides through processes such as

titanium in-diffusion or proton exchange [90].

This leaves a single alternative, physical etching. Inspired by Refs. [83, 85, 91], we processed our lithium niobate using argon ion beam etching (also called ion milling) in an inductively coupled plasma etcher. However, ion milling lithium niobate causes amorphous LN redeposition, creating unwanted features and increasing sidewall roughness as seen in Fig. 2.7 (a,b). We mitigated this problem first by optimizing the plasma etching parameters to minimize redeposition and then by chemically cleaning our sample. The results are shown in Fig. 2.7 (c). The chemical cleaning step used based on RCA-1, which is typically used on silicon devices [92] and found to be effective on lithium niobate [93].

2.3.2 Nanofabrication Procedure

The fabrication of the lithium niobate resonators was performed in the cleanroom of the Van Leeuwenhoek Laboratory in Delft. Our process places electrodes on top of the lithium niobate first and then etches resonators into the lithium niobate. We use the first of two electron-beam lithography steps to define the pattern of our IDT. Then we deposit gold and perform liftoff. In the final four steps, we create our resonator structures. Our second beamwrite defines the geometry of our resonators. We use an ion mill to etch this design into the lithium niobate. The structures are released using a reactive ion etch. Finally, we use an inorganic clean to counteract the unwanted effects of argon milling described above.

We begin our fabrication using 5 mm by 10 mm chips diced from a four-inch Lithium Niobate on Silicon (LNOS) wafer. Our wafer was acquired from NGK Insulators, Ltd. and consists of 340 nm layer of X-cut, single crystal lithium niobate doped with 5mol% MgO bonded to a 500 μm thick silicon substrate (the thickness of the LN varies $\pm$10 nm over the scale of the wafer). Our fabrication consists of eight process steps, shown in Fig. 2.8:

1) Spin Resist. We spin our resist, CSAR-62.09, to a thickness of 280 nm.

2) E-Beam Exposure. Then, the first beamwrite defines the deposition of metal that makes up the pads and IDTs. All lithography was done with a Raith 5200 Electron Beam Pattern Generator. We develop the exposed pattern by submerging the chip in beakers of pentyl-acetate, 1:1 MIBK:IPA, and IPA for one minute each.

3) Gold Evaporation. The next step is metal deposition, where we create our electrodes using a Temescal FC-2000 electron-beam evaporator. We deposit a metal stack

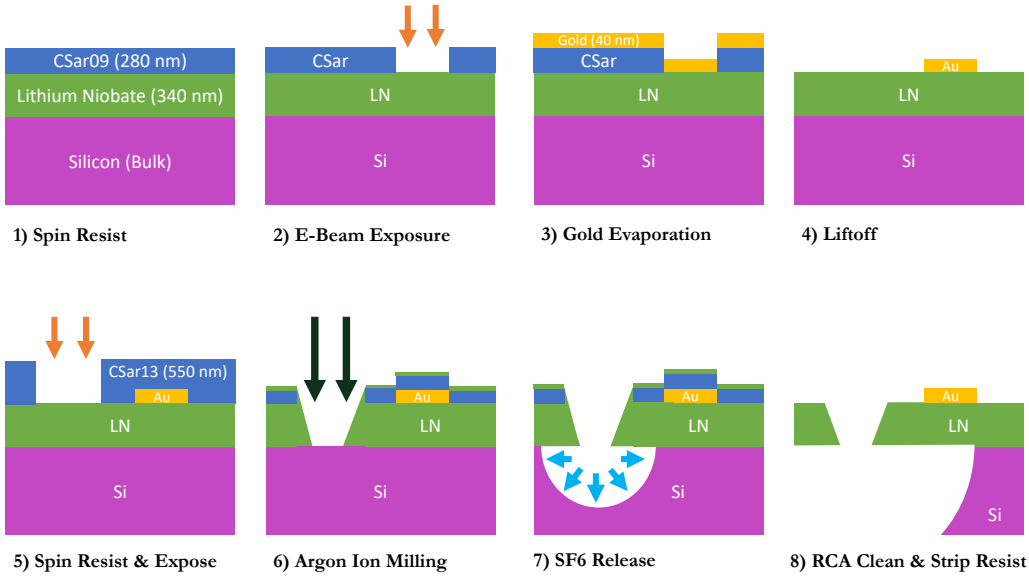

Figure 2.8: ***Fabrication Flow.*** *The steps of our fabrication process are laid out. Orange arrows in steps two and five indicate exposure with an electron beam, dark green arrows indicate physical etching with argon ion beam, and blue arrows indicate chemical etching with* SF_6.

consisting of 5 nm of Chromium, 15 nm of Platinum, and 40 nm of gold.

4) Liftoff. Then, we lift off the metal on the previously unexposed areas in a bath of 70° C Anisole placed into an ultrasonic bath for 3-5 minutes.

5) Spin Resist and Expose. After rinsing the device with acetone and IPA, we perform a second electron-beam lithography step to define an etch mask. This time, CSAR-62.13 is spun to a thickness of 550 nm. Thicker resist is required because the ion milling process etches the resist approximately as fast as the lithium niobate. After the resonator patterns are defined, the chip is developed again in pentyl-acetate, 1:1 MIBK:IPA, and IPA.

6) Argon Ion Milling. Then the chip is placed in an SCIA Ion Mill 150. The exposed lithium niobate film is etched through by a large cross-sectional beam of argon ions incident at a 90-degree angle to the surface of the chip, which rotates at 10 rpm for 45 minutes. We got the best results when the source (or plasma) and the bias (or beam) voltages were set to 100 and 400 volts, respectively. While this process etches fully through the lithium niobate film, it also results in the redeposition of material shown in Fig. 2.7.

7) SF_6 **Release.** After ion milling, there is still resist residue on the non-etched areas of the chip. In order to avoid gold contamination of the etcher, we chose to leave the resist and redeposited lithium niobate on our devices while we underetch the silicon in an Alcatel AMS 100 I-speeder using an SF_6 chemistry at $-10°$ C, which results in an isotropic undercut of more than 5 microns.

8) RCA Clean and Strip Resist. Next, we remove the resist by placing the sample in a beaker of 80° C di-methylformamide (DMF) for 5 minutes, rinsing with IPA, and then ashing in oxygen plasma. Ashing is done in a PVA Tepla 300 where we set the O_2 flow to 200 sccm and the RF bias voltage to 300 V. The resist may be difficult to remove because the bombardment of argon ions burns some resist onto the lithium niobate layer of our samples. It is possible that only one of these steps is strictly necessary to remove resist, but we found resist residue on our samples in SEM images unless we did both. Finally, we employ an inorganic cleaning step to remove redeposited lithium niobate. We prepare a mixture similar to RCA-1, using a 2:2:1 ratio of $NH_4OH[28\%] : H_2O_2[31\%] : H_2O$, heat it to 85° C and mix with a stir bar for 5 minutes, and then place our samples in for an additional 5 minutes. This weak wet etch removes LN at a rate of 6.7 nanometers per minute.

2.4 Measurements

We made over a dozen iterations of thin film resonators over the course of this project, and it would be impractical to show all of the data that was collected. Instead, we will begin by carefully analyzing a single device, and then comparing it to more complex generations of devices. All devices were patterned with the electrodes wired to large pads in a ground-signal-ground (GSG) configuration. They were measured in reflection by a coaxial RF GSG probe (FMPB1000 from Fairview Microwave) connected via SMA cable to a Vector Network Analyzer (VNA). We normalized the reflection measured by the VNA (Rohde & Schwarz ZNB40) to the open response of the probe. We did not impedance match our devices, and we expect all of our structures to be undercoupled based on the analysis of Ref. [94].

We will first examine a simple resonator in order to gain a good understanding of what can be learn from reflection measurements of our devices. We measure the device shown in Fig. 2.9 (a), which was fabricated on X-cut lithium niobate with the direction of propagation along the Y-axis. It consists of a 20 micron wide by 5 micron long slab, bulging out in the

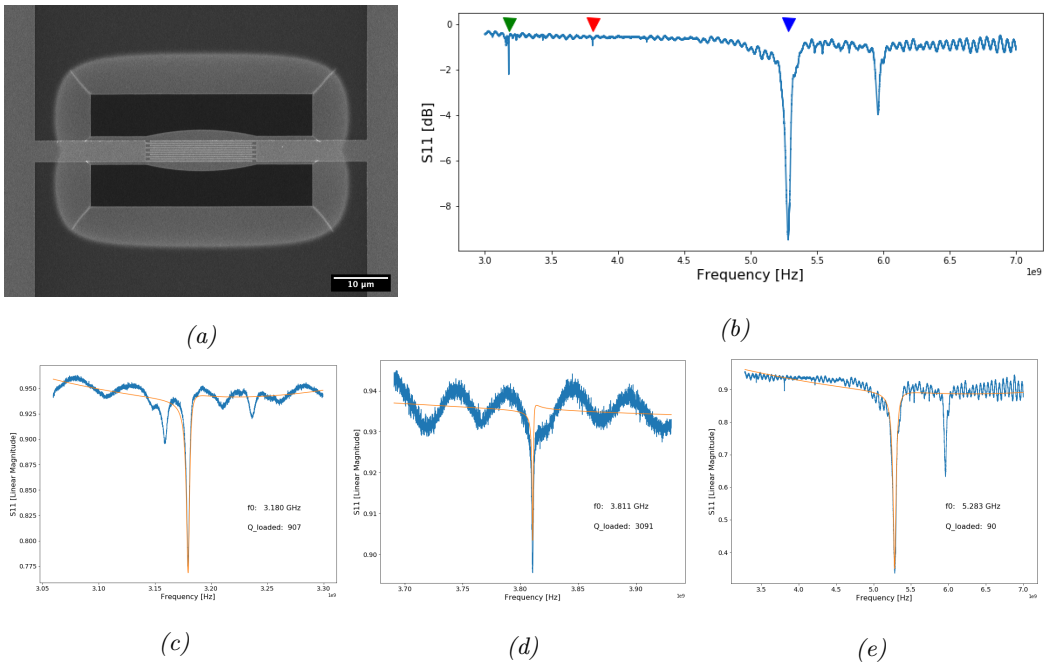

Figure 2.9: ***The Thin Film BAW Modes of a Resonator.*** *(a) A SEM image of a thin film BAW resonator. (b) The reflection spectrum of this device from 3-7 GHz. The S0, A0, and SH0 modes are indicated under green, red, and blue arrows, respectively. (c,d,e) show the fitted linewidths of S0, A0, and SH0 modes, respectively.*

longitudinal direction by 1.5 microns. These dimensions are identical to the device simulated in Section 2.2. The curvature was intended to confine the motion of the resonator to the center in order to lower the mode volume, which will be discussed later on in Sec. 2.4.1. On top, we patterned a 10-finger IDT with a pitch of .35 microns.

Based on the analysis conducted in Sec. 2.2.2, we attempt to match the three prominent dips in the reflection spectrum shown in Fig. 2.9 (b) to their corresponding bulk acoustic modes. We designed this device to have an IDT with many fingers which should only strongly excite one longitudinal order of each BAW mode, which makes distinguishing the modes easier to distinguish from each other. We could use Transmission-mode Microwave Impedance Microscopy (TMIM), a technique that can measure the displacement profiles of modes in real space, to label our modes with certainty [95]. However, we did not have access to this tool during this project.

We expect the lamb wave modes S0 and A0 to be at a lower frequency than the shear wave mode SH0. We also expect SH0 to have the largest electromechanical coupling ($K^2 \approx 22\%$) followed by S0 ($K^2 \approx 10\%$), both of which are much larger than A0 ($K^2 \approx 3\%$). The larger electromechanical coupling corresponds to a larger dip depth of modes in the graph. Finally, these modes match their simulated frequencies fairly well - we measured (simulated) the frequency of S0 to be 3.18 (3.21) GHz, A0 to be 3.81 (3.34) GHz, and SH0 to be 5.28 (5.05) GHz. We see that only A0 differs significantly from its simulated frequency. This is likely due to its out-of-plane motion, the frequency of A0 is far more sensitive to changes in the thickness of the film. We simulated a film thickness of 300 nanometers, but because of the electrodes (between 50 - 100 nm) patterned on top, the thickness of the measured device was probably larger than that.

Each of the three discussed modes are plotted in more detail and fit to a Lorentzian lineshape in Fig. 2.9 (c,d,e). We found that on this device, the S0, A0, and SH0 modes had a loaded quality factor of 907, 3091, and 90, respectively. We consider the figures of merit of a state-of-the-art device to be Q factors above 2500 and electromechanical coupling over 10 percent (based on the broader overviews of similar devices conducted in Refs. [81, 82]).

The biggest surprise here is that the SH0 mode displays a very poor effective quality factor. There are many things that could cause this, but we suppose that the main contributing factor is that the SH0 mode consists of transverse expansion and contraction (as opposed to the longitudinal motion of the lamb wave modes). Therefore, despite the large electromechanical coupling displayed by the mode, the large losses make this mode undesirable for this device. We suspect that these losses are caused both the wide tether and the curved edge of the film, features which encourage transverse instead of longitudinal confinement. The shear mode linewidth appeared extremely broad in all devices we tested, including some with no curved edges, indicating that the rounding was not solely responsible for the low Q factor of SH0 modes. There are ways to mitigate these factors that can still be explored, such as replacing our tethers with a phononic shield. However, in this work we decided to focus our efforts on the lamb wave modes instead.

While the very large quality factor of the A0 mode is encouraging, the low k^2 (barely larger than spurious modes) makes it less desirable than S0 for use in an efficient transducer. Moving forward, we attempted to optimize the S0 mode by raising the Q factor and k^2 and further explore how the resonators could be combined with slapped photonic crystal

nanobeams for applications in microwave to optical conversion. At this point, we still had many questions about our devices. How many resonators can one fit on one device? How does the curvature of the resonator affect the quality factor of each mode? Which angle of propagation is best for each mode? We searched for answers to these questions and more by designing and measuring many variations of these devices. We briefly recap our findings in the remainder of this section.

2.4.1 Dependence on Resonator Curvature

One of our design goals is to lower the effective mass of the acoustic mode as much as possible. Our idea was to achieve this by curving one or both of the long edges of the resonator. We found in our COMSOL simulations that curving this edge by even a small amount confines the longitudinal motion of the lamb wave modes to the center of the resonator. This also had the effect of increasing the quality factor of these modes by about a factor of about two, indicating that the confinement could also lead to reduced scattering losses. In addition we found that sweeping the radius of curvature resulted in roughly similar confinement, leading us to conclude that the amount of curvature doesn't seem to matter much.

These observations were loosely verified by experimental tests. Fig. 2.10 shows the suspected S0 mode of two resonators from the same chip, identical except that the device shown in (a) has no curvature, and the device shown in (c) has a large radius of curvature. Indeed, we see that the loaded quality factor of the straight-walled resonator is 434 while the rounded resonator's is 1102. It seems that the curved resonator is better at confining the S0 mode than one without curvature - however, this is hardly surprising when we consider that the thin film resonator is tethered by a thick strip which is as wide as the resonator. Using multiple, thinner tethers in future devices, we were able to achieve higher quality factors in curvature-free devices. This observation does not confirm that curvature of the edges actually makes the effective mass smaller. Using TMIM on this sample could be used to measure the displacement of the modes in real space and thus better our understanding of the confining effects of curving the resonator edges.

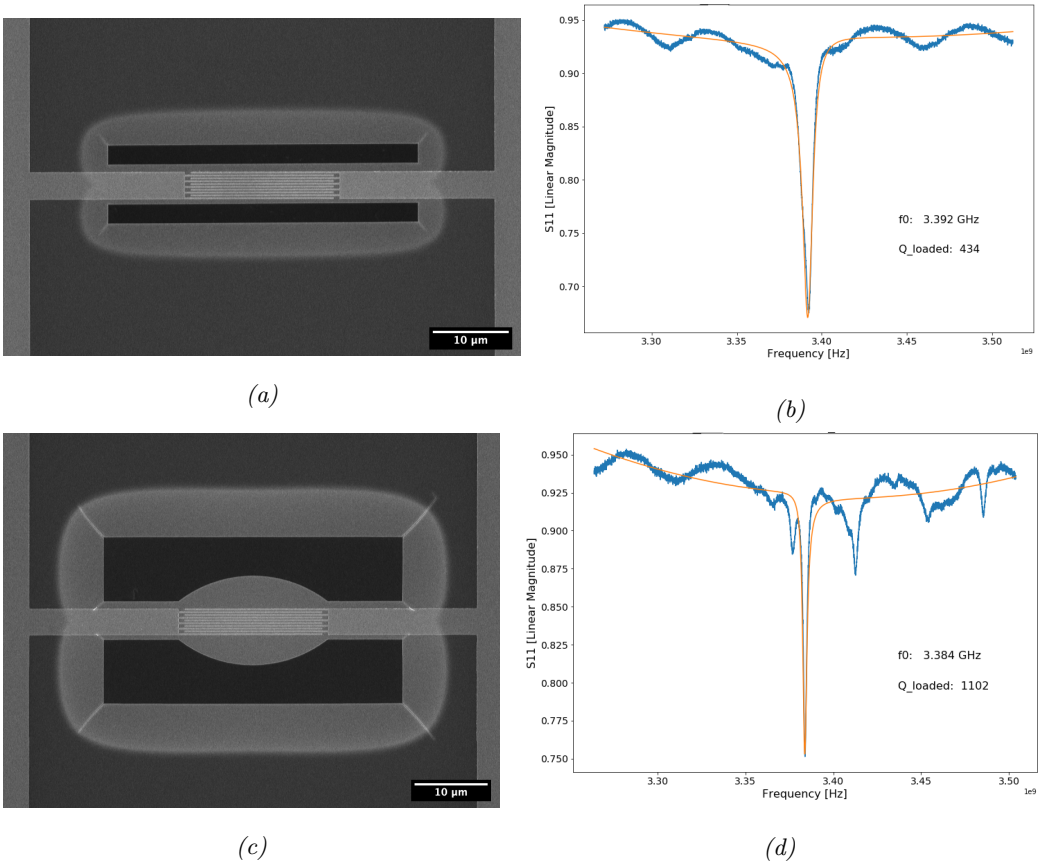

Figure 2.10: ***The Effect of Resonator Curvature.*** *(a) A SEM image of a resonator with straight sides. (b) A fitted reflection spectrum of a suspected S0 mode at 3.39 GHz from this device. (c) A SEM image of a device with sides displaying a large radius of curvature. (d) A fitted reflection spectrum of a suspected S0 mode at 3.38 GHz from this device. The curvature of the resonator sides seems to raise the quality factor of the S0 mode.*

2.4.2 Multiplexing Thin Film Devices

We were curious to see whether we could measure multiple resonators with a single VNA scan, which would allow us to fit more resonators on a single chip. We designed a multiplexed device, shown in Fig. 2.11 (a), comprised of three resonators connected to the same GSG pads. The leftmost is identical to the center except that it is scaled down by five percent, and the rightmost is identical to the center except scaled up by five percent. This

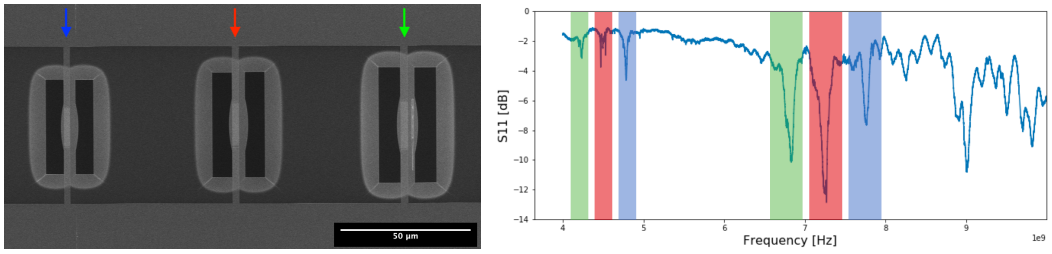

(a) *(b)*

Figure 2.11: ***Multiplexing Thin Film Resonators.*** *(a) A SEM image a multiplexed device. The colored arrows are added labels. (b) A reflection measurement of all three resonators. Each shaded color labels a grouping of resonances. The colors correspond to the labels of three resonators in (a).*

is in order to give the devices sufficiently different center frequencies that their signals were easily distinguishable. The results, shown in Fig. 2.11 (b), were clearly successful - we see three groupings of similar features, approximately 500 MHz apart from one another. These groups are shaded the same color in the plot

At this point, we made three adjustments to the design. Simulations of resonators with nanobeams on top indicated that having an acoustic wavelength close to the width of the nanobeam increased optomechanical coupling, so we increased the pitch of our IDTs in order to lower the frequency. We also aimed to reduce the effective mass of our mode, which increases the optomechanical coupling rate. This was accomplished by decreasing the number of IDT fingers from ten to four. Because IDT bandwidth is inversely proportional to the number of finger pairs, smaller IDTs excite several A0 and S0 modes of different longitudinal orders at once. This ultimately results in the spectra getting more crowded, making it much more difficult to confidently distinguish between A0 and S0 resonances. This is inconvenient for studying the spectra in this chapter but will not hinder our goal of a proof-of-concept transduction measurement. Finally, our simulations indicate that using one curved edge had the same confining effects as curving both, so we slimmed down one side of the resonator in a further attempt to lower the effective mass.

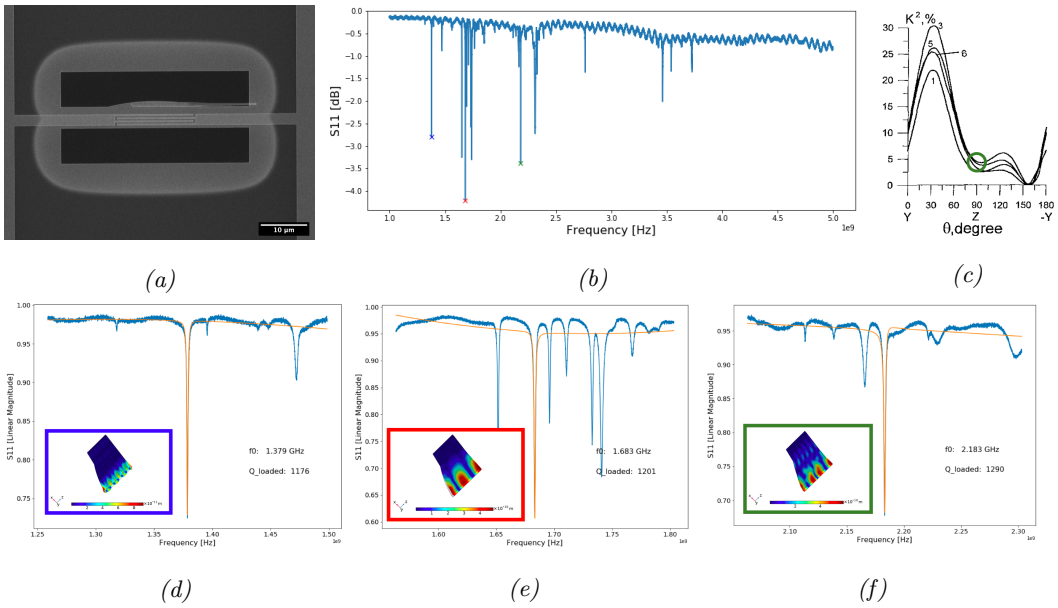

Figure 2.12: ***Changing the Resonator Direction of Propagation.*** *(a) A SEM of a device where acoustic propagation is in the crystal Z direction. The nanobeam visible in the SEM image was added after these measurements were taken and is irrelevant to this section. (b) The reflection spectrum of this device. (c) The theoretical value K^2 plotted as a function of propagation angle, with the device's parameters circled in green. The three modes with the highest quality factor are indicated by crosses. Graph reproduced from [88]. (d,e,f) The dips marked with blue, red, and green in the full spectrum are plotted individually. The insets show a COMSOL simulation of the presumed displacement profile of each mode.*

2.4.3 Dependence on Angle of BAW Propagation

In next two generations of chips, we continued the search for optimized S0 modes by varying the direction of propagation. We tried rotating our resonators 90 degrees so that the direction of propagation from the IDTs was in the crystal Z direction. Fig. 2.12 shows a SEM image of such a device in (a) and the corresponding reflection spectrum in (b). We see a litany of peaks with moderate dip depth, which is unsurprising when we examine the angular dependence of the intrinsic electromechanical coupling (Fig. 2.12 (c)) and find that the maximum electromechanical coupling drops from 10 to 5 percent for the S0 mode in

these devices. However, we were able to find several modes with a relatively high quality factor. Using COMSOL simulations, we attempted to match the high Q modes to their respective lamb waves. We suspect that we found three zeroth-order lamb wave modes with loaded Q's over 1000.

In order to increase our confidence in mode identification, we investigate the Free Spectral Range (FSR) of the resonator. In this case, we define the FSR to be $\Delta f_{FSR} = \frac{v_p}{2L}$ where v_p is the phase velocity and L is the length of the cavity. This device has L = 5.5 μm. We can use information to quickly validate our measurements with our simulations and theoretical predictions. According to Ref. [88], the phase velocities of each mode in our device are $v_{p,A0} = 3000$ m/s and $v_{p,S0} = 6700$ m/s. This corresponds to $\Delta f_{FSR,A0} = 270MHz$ and $\Delta f_{FSR,S0} = 610MHz$. In our simulations, we find A0 modes with $\Delta f_{FSR} \approx 300$ MHz and S0 modes with $\Delta f_{FSR} \approx 660$ MHz. The spectrum in Fig. 2.12 (b) shows two evenly spaced of modes, with FSRs of 300 and 690 MHz. We use the rough agreement between measured, simulated, and predicted FSRs to make educated guesses about which mode is which. We measured (simulated) and attempted to label the following resonances: an A0 mode at 1.39 (1.44) GHz with a Q of 1176, a S0 mode at 1.68 (1.49) GHz with a Q of 1201, and another S0 mode at 2.18 (2.21) GHz with a Q of 1290. These three modes are shown in Fig. 2.12 (d,e,f).

In the next generation of devices we tested out another propagation angle to search for devices with higher Q factors. One is tempted to use the angle that maximizes the K^2 of S0, 30 degrees from the y-axis. However, Ref. [81] reports that losses to the spurious mode A0 limit the quality factor of S0 modes at this angle. Instead, we carefully study the theoretical maximum electromechanical coupling of the S0 and A0 modes in X-cut LN and see that there is a specific angle where the A0 mode cannot couple, indicated respectively in Fig. 2.13 (b) and (c). Following Ref. [96], we align our angle of propagation close to this angle, 60 degrees from the y-axis. In theory, less energy will couple into the A0 modes, leading to lower losses and thus higher Q factors of the S0 modes. The device shown in Fig. 2.13 (a) had three resonances with loaded quality factors over 2500, marked in Fig. 2.13 (d) by colored crosses. These resonances, shown in Fig. 2.13 (e,f,g) have resonances at 1.17, 2.03, and 2.55 GHz with quality factors of 2653, 5254, and 3041, respectively. Unfortunately, we don't feel like we can conclusively match these resonances to simulated modes.

While these devices yielded interesting results and several high quality factor modes, their

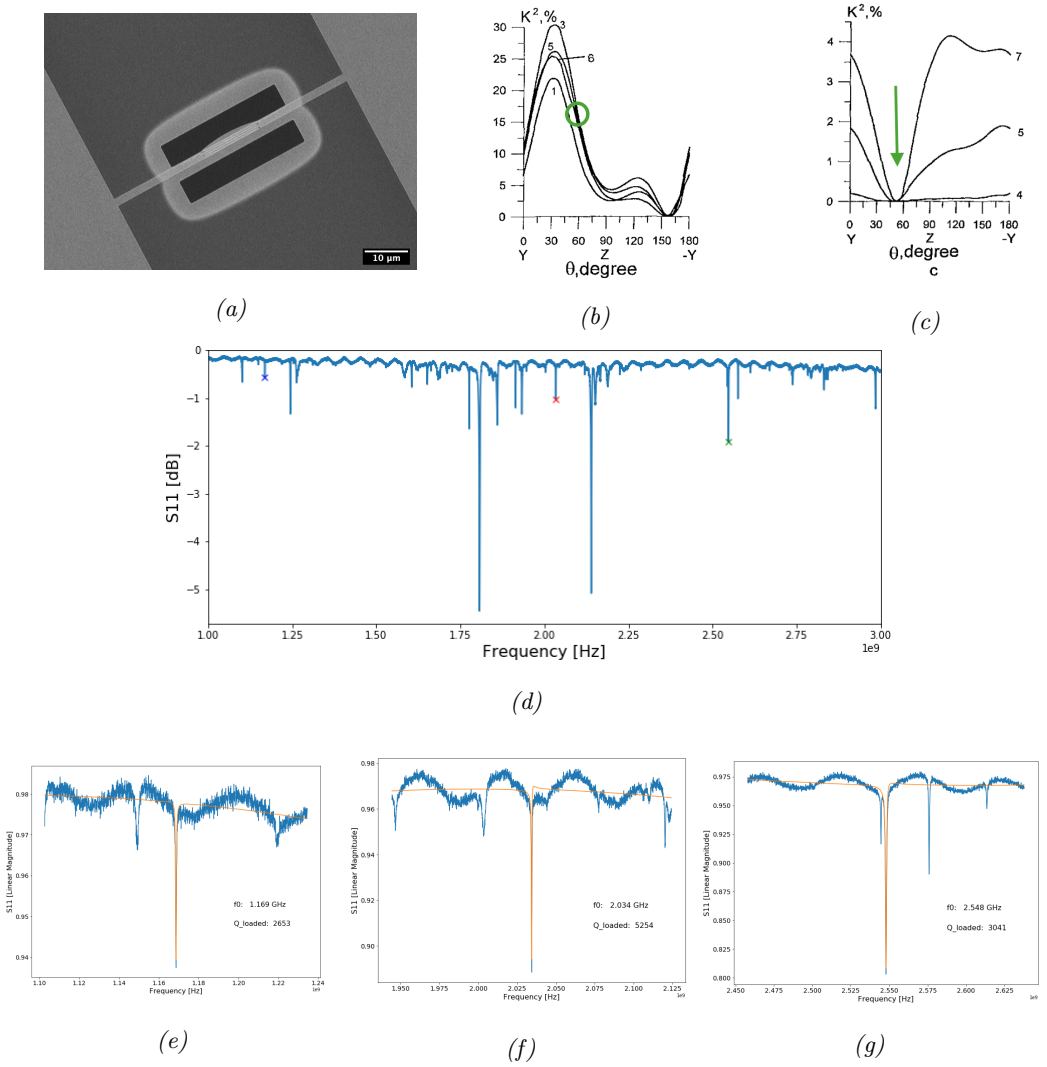

Figure 2.13: ***Further Changing the Resonator Direction of Propagation.*** *(a) A SEM of a device where acoustic propagation is +60° w.r.t. the crystal Y direction. In (b,c), theoretical maximum intrinsic electromechanical coupling of the S0 and A0 modes, respectively are plotted as a function of propagation angle, with the device's parameters marked in green. (b,c) are reproduced from [88]. (d) Reflection spectrum of this device. The dips marked with blue, red, and green are plotted individually and fitted in (e,f,g), respectively.*

electromechanical properties are still not optimized for maximal transduction efficiency. In the future, we will continue exploring different device orientations and resonator geometries. In addition, we would like to carefully consider the optimal thickness of the film and the structure of the IDTs in order to engineer the dispersion of the S0 and A0 modes. However, the goal of our investigation was to execute a proof-of-concept of transduction measurement and we felt that we had created devices with good enough properties to see some transduction effects. The rest of our efforts were directed towards placing silicon optomechanical crystals on lithium niobate, discussed in the next chapter.

2.4.4 Next Steps

In this section, we designed and demonstrated thin film BAW resonators for use in a transduction experiment. After reviewing the piezoelectric properties of lithium niobate, the different classes of acoustic resonators, and the acoustic waves that propagate in such devices, we designed and simulated a thin film device in which an IDT actuates GHz BAW modes. Then, we learned how to fabricate such devices in our cleanroom where we grappled with the issue of etching lithium niobate. We then measured the reflection spectra of our devices and found them to be capable of exciting modes with quality factors over 5000. We found these resonators suitable for the purpose of a proof-of-concept transduction measurement.

There are many things we could have spent more time on to further develop our resonator design. As noted, the most obvious improvement would be to fabricate devices with an optimized angle of propagation in order to maximize K^2. Additionally, more work in simulating and measuring the k^2 of our devices would lead to further improvement. One way to move forward is to make use the modified Butterworth-Van Dyke model to impedance match the devices to a fifty ohm port and measuring the admittance of devices to experimentally recover the exact value of k^2.

There is also progress to be made in the design of the devices. More research into the way that curvature (or more complex shapes) confine acoustic modes in the thin film would be welcomed. Further understanding of how acoustic energy is lost through the tethers could lead to devices with a substantially higher quality factor. This could involve a simple re-design of the tethers or a more complex design that surrounds the device with a phononic shield. Furthermore, one could investigate making devices optimized for the SH0-mode -

this mode also has very large maximum K^2 and perhaps there is a design that can better provide better optomechanical coupling when combined with a photonic crystal cavity.

Lastly, we are interested in the properties of these resonators when they are cooled down to subkelvin temperatures. We suspect that cooling the devices will lead to substantially higher quality factors as various loss channels are frozen out.

Chapter 3

Hybrid Piezo-Optomechanical Silicon-on-$LiNbO_3$ Devices

The goal of this project is to measure piezo-optomechanical transduction with slapped nanobeams. In the previous two chapters, we have developed the technique of slapping and designed a lithium niobate electromechanical resonator suitable for wavelength conversion. Now we put everything together to create our transducer. First, we explain the details of our piezo-optomechanical transduction strategy in Section 3.1. In Section 3.2, we simulate and fabricate silicon photonic crystal cavity nanobeams developed to be slapped on top of our lithium niobate resonator. Finally, a transduction device is designed in Section 3.3 and measured and analyzed in Section 3.4.

3.1 Piezo-Optomechanical Transduction

When you use the internet on your phone or computer, your device retrieves RF electrical information from distant servers at incredible speed. This is made possible by modern telecommunication networks which use optical laser light to send RF signals around the world. The Electro-Optic Modulator (EOM) is the workhorse technology that makes this possible. EOMs are usually centimeter-scale nonlinear crystals with electrodes driven by RF voltages that modulate the phase (or, in different configurations, the amplitude or intensity)

of a laser beam by means of the Pockels Effect. These devices operate using classical signals and can have efficiencies on the order of $\eta = 10^{-10}$ [97] - not an issue in classical networks, but unsuitable for quantum communications which cannot tolerate large losses.

3.1.1 Classical vs. Quantum Wavelength Conversion

Efficient quantum microwave to optical transduction is a challenge with very different requirements from the classical case. Classical modulators operate at room temperature, while quantum wavelength conversion will take place at cryogenic temperatures. Classical modulators are mostly broadband, while the fixed frequency of qubits means that quantum converters can have extremely small bandwidths [11]. Classical transducers are 'continuous' devices, meaning that the laser and the RF drive operate simultaneously for long durations. In contrast, quantum transduction using a mechanical resonator will probably be 'pulsed.' First, microwave pulses will transfer an excitation from a superconducting circuit to a mechanical resonator. Then, a pulsed optical laser drive will read out the state of the mechanical resonator. Optical to microwave conversion is achieved by the reverse process.

There are several reasons to use a pulsed scheme. Crucially, this strategy conducts the electromechanical and optomechanical interactions separately, which avoids absorption issues that are introduced when superconducting circuits operate in the presence of optical light. In addition, the mechanical resonator must be cooled to sub-phonon occupation before conversion can begin. If the laser drive was continuous the mechanical element would heat up, but pulsed operation allows for rethermalization after each cycle. The mechanical resonator can be cryogenically initialized in its ground state given enough time in between pulse cycles when $\hbar\Omega_m > k_B T$, a condition met by operation at hypersonic frequencies (> 1 GHz) and dilution refrigerator temperatures (≈ 10 mK). Finally, pulsed conversion does not require the bandwidths of the optical and microwave resonators to be matched [39]. At present there is ongoing research into a litany of different approaches to develop such a converter. In the introduction, we reviewed some of these and motivated our focus on piezo-optomechanical techniques. We note that a near comprehensive review of comparisons between similar experiments is found in Table 1 of Ref. [23] (excluding [39], which was published later).

Typically, piezo-optomechanical transducers are developed in two stages. First, the de-

vices are fabricated and measured continuously as classical modulators at room temperature. At this stage, the properties of the optical and mechanical resonators are measured and the optomechanical and electromechanical coupling strengths are determined. We were able to reach this point in our project. After designing a promising converter, the device can be cooled down and connected to a superconducting circuit in order to measure pulsed quantum wavelength conversion. Finally, spectroscopy, sideband thermometry, and pulsed operation establishes the added noise, repetition rate, and quantum efficiency of the transducer. The motivation for this experiment is to reach this stage with our devices in the future.

3.1.2 Fundamentals of Optomechanics

In order to understand our transducer, we examine the often-studied cavity quantum optomechanics model [30]. We start with a Hamiltonian describing an uncoupled optical cavity mode and mechanical harmonic oscillator at frequencies ω_c, Ω_m and with creation/annihilation operators $\hat{a}^\dagger/\hat{a}, \hat{b}^\dagger/\hat{b}$, respectively.

$$\hat{H} = \hbar\omega_c \hat{a}^\dagger \hat{a} + \hbar\Omega_m \hat{b}^\dagger \hat{b} \tag{3.1}$$

If we add parametric coupling between the optical mode and the position of the mechanical element (assume $\omega_c = \omega_c(x)$) and expand about the equilibrium position of the mechanical resonator up to the linear term, we find

$$\hat{H} = \hbar\Big(\omega_c(0) + \hat{x}\frac{\partial\omega_c(x)}{\partial x}\Big|_{x=0}\Big)\hat{a}^\dagger\hat{a} + \hbar\Omega_m\hat{b}^\dagger\hat{b} \tag{3.2}$$

The second quantization of position gives the relationship $\hat{x} = \sqrt{\frac{\hbar}{2m_{eff}\Omega_m}}(\hat{b}^\dagger + \hat{b}) = x_{zpf}(\hat{b}^\dagger + \hat{b})$ where m_{eff} is the effective mass of the mechanical mode and $x_{zpf} = \sqrt{\frac{\hbar}{2m_{eff}\Omega_m}}$ is the zero point fluctuations of the position operator. Substitution yields

$$\hat{H} = \hbar\omega_c\hat{a}^\dagger\hat{a} + \hbar\Omega_m\hat{b}^\dagger\hat{b} + \hbar x_{zpf}\frac{\partial\omega_c(x)}{\partial x}\Big|_{x=0}\hat{a}^\dagger\hat{a}\Big(\hat{b}^\dagger + \hat{b}\Big) \tag{3.3}$$

This Hamiltonian is a model of a photonic cavity with one mirror attached to a mechanical resonator, displayed in Fig. 3.1 (a). The motion of the mechanical element changes the cavity length and modulates the frequency of the light while optical radiation pressure forces act on the mechanical resonator. Finally, we define the single photon optomechanical

coupling rate $g_0 = x_{zpf}\partial\omega_c(x)/\partial x|_{x=0}$ as the shift in the optical cavity frequency equal to the displacement of the mirror by x_{zpf}. Now we recover the interaction Hamiltonian

$$\hat{H}_{int} = \hbar g_0 \hat{a}^\dagger \hat{a}\left(\hat{b}^\dagger + \hat{b}\right) \tag{3.4}$$

We want to understand what happens when the system is driven by a laser at frequency ω_d detuned from the cavity by $\Delta = \omega_d - \omega_c$. Therefore it is convenient to transform the Hamiltonian to a frame rotating at the drive frequency by applying $\hat{U} = \exp[i\omega_d t\hat{a}^\dagger\hat{a}]$.

$$\hat{H} = -\hbar\Delta\hat{a}^\dagger\hat{a} + \hbar\Omega_m\hat{b}^\dagger\hat{b} + \hbar g_0\hat{a}^\dagger\hat{a}\left(\hat{b}^\dagger + \hat{b}\right) \tag{3.5}$$

In practical experiments, the total mechanical loss rate Γ_m is larger than the optical cavity losses (κ) and g_0, so the system is always in the weak coupling regime. Therefore, we can attempt to linearize our Hamiltonian by setting $\hat{a} = \bar{a} + \partial\hat{a}$, where $\bar{a}$ is the average classical drive amplitude and $\partial\hat{a}$ are fluctuations. This yields an interaction term

$$\hat{H}_{int} = \hbar g_0\left(\bar{a} + \partial\hat{a}\right)^\dagger\left(\bar{a} + \partial\hat{a}\right)\left(\hat{b}^\dagger + \hat{b}\right) \tag{3.6}$$

We proceed using $\partial\hat{a} = \hat{a}$ to simplify notation. Multiplying the two leftmost brackets breaks the interaction Hamiltonian into four terms. The term that is proportional to the intracavity photon number $\bar{a}^2 = n_{cav}$ contains no creation or annihilation operators of the optical cavity. The result in a static shift of the equilibrium position of the mechanical oscillator which can be accounted for by using an effective detuning. Another term in the interaction is proportional to $\hat{a}^\dagger\hat{a}$, which contains no factor of $\bar{a}$ and thus can be neglected. The others two terms, of order $|\bar{a}|$, give us our linear interaction Hamiltonian:

$$\hat{H}_{int} = \hbar g_0\sqrt{n_{cav}}\left(\hat{a}^\dagger + \hat{a}\right)\left(\hat{b}^\dagger + \hat{b}\right) \tag{3.7}$$

Note that the interaction rate $g = g_0\sqrt{n_{cav}}$ is enhanced by increasing the drive intensity. In the resolved sideband limit $\Omega_m \gg \kappa$ where the mechanical frequency is greater than the optical cavity losses, there are two especially useful cases, illustrated in Fig 3.1 (b). If we set the detuning equal to the mechanical frequency ($\Delta = \Omega_m$) and use the rotating wave approximation, we find

$$\hat{H}_{TMS} = \hbar g\left(\hat{a}^\dagger\hat{b}^\dagger + \hat{a}\hat{b}\right) \tag{3.8}$$

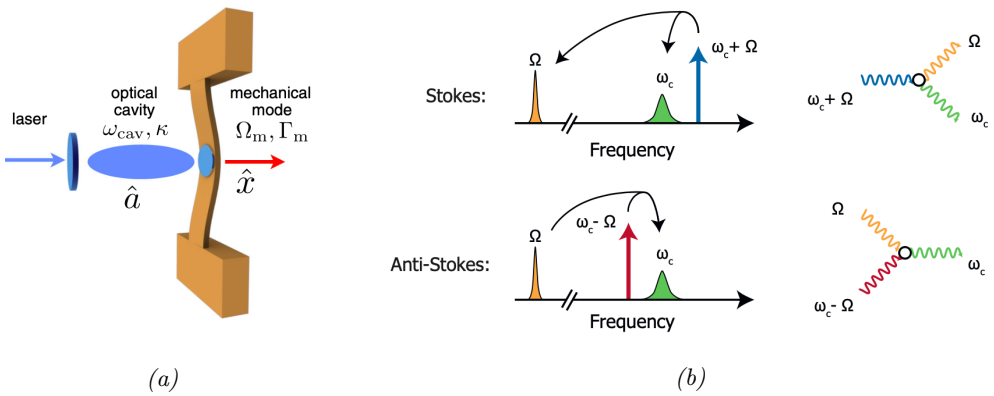

Figure 3.1: ***Optomechanics.*** *(a) Model optomechanical system of an optical cavity with a movable mirror. (b) The linearized interactions of the cavity optomechanics Hamiltonian. A frequency space diagram of the stokes (anti-stokes) process where the optical drive is detuned by the mechanical frequency to the blue (red) side of the optical cavity is displayed on top (bottom) in frequency space. To the right of each is the corresponding Feynman diagram. Images (a,b) are taken from Refs. [30, 49], respectively.*

This 'two-mode squeezing' Hamiltonian describes a stokes-like process which creates and annihilates a pair of excitations in the optical and mechanical resonator. When the mechanical oscillator is in its ground state, light at the cavity drive frequency $\omega_d = \omega_c + \Omega_m$ can simultaneously create an entangled photon-phonon pair at frequencies ω_c and Ω_m, respectively.

The other useful interaction is the 'beam-splitter' Hamiltonian, where the detuning is set to the red sideband instead of the blue one ($\Delta = -\Omega_m$).

$$\hat{H}_{BS} = \hbar g\left(\hat{a}^\dagger \hat{b} + \hat{a}\hat{b}^\dagger\right) \tag{3.9}$$

This anti-stokes process effectively swaps an excitation from the optical cavity mode to the mechanical resonator mode, and vice versa. The red and blue sideband interactions result in three-wave mixing that up- or down-convert drive photons into cavity photons.

While studying the linearized interaction Hamiltonian helps build intuition for optomechanical systems, the feedback dynamics of the system more complex. This system exhibits radiation-pressure induced back-action: as the mechanical motion shifts, the optical cavity the optical intensity shifts which changes the force experienced by the mechanical oscillator.

In the literature, the dynamics are often recovered by solving the following semi-classical Langevin equations using an input-output formalism [30, 43]:

$$\dot{\hat{a}} = \Big(i\Delta - \frac{\kappa}{2}\Big)\hat{a} - ig_0\hat{a}\Big(\hat{b} + \hat{b}^\dagger\Big) + \sqrt{\kappa_e}a_{in} \tag{3.10}$$

$$\dot{\hat{b}} = -\Big(i\Omega_m + \frac{\gamma}{2}\Big)\hat{b} - ig_0\hat{a}^\dagger\hat{a} + \sqrt{\gamma_e}b_{in} \tag{3.11}$$

where $\kappa = \kappa_i + \kappa_e$, $\gamma = \gamma_i + \gamma_e$ are the total, intrinsic, and external loss rates of the optical and mechanical resonators, respectively. These equations can be solved by Fourier transform methods under appropriate conditions. Then, the scattering parameters of the input and output ports can be written in terms of the solved Heisenberg operators. We use this approach in Appendix A to relate our measurements to figures-of-merit relevant to wavelength conversion.

3.2 Silicon OMCs on Lithium Niobate

In the previous chapter, we designed a piezoelectric resonator. Now, we turn our attention to a compatible optical cavity. There are many designs to choose from. Our device requirements are the following:

1) High Performance: An important figure-of-merit of our OMCs is the optomechanical single-photon cooperativity, $C_{0,om} = \frac{4g_0}{\kappa\gamma}$. We aim to we need to maximize the single-photon optomechanical coupling rate while minimizing the optical and mechanical loss rates. An additional objective is reaching the resolved sideband regime, $\Omega_m > \kappa$, where the mechanical frequency is greater than the optical losses.

2) Efficient Coupling: Efficiency conversion only works if we are capable of getting light in and out of the cavity with low optical losses. We therefore require the system to have near unity optical coupling efficiency $\eta_{oc} \approx 1$.

3) Slappable: We want to make our devices using the slapping technique described in Chapter 1. Therefore the cavity can be made of any material as long as it survives the slapping procedure.

4) Wavelength: We want our optical cavity to operate in the telecom bands around 1550 nanometers in order send optical information through ultra-low loss fiber networks. In

addition, high mechanical frequencies ($> 1GHz$) are preferable because they can be cooled to their motional ground state at dilution refrigerator temperatures.

Optomechanical crystal nanobeams are an excellent candidate, as they fulfill all of these requirements. The devices operate in the correct frequency range. Input and output coupling efficiencies can approach unity using carefully engineered tapered fiber coupling methods [41, 49, 51, 52]. Furthermore, in Chapter 1 we have shown that OMC nanobeams can be slapped successfully.

Finally, we must choose the material of our OMCs. The main consideration is that our nanobeams will be placed on top of lithium niobate. We therefore need our nanobeams to be made of a material that will have sufficient refractive index contrast with lithium niobate (n=2.21 at 1550 nm) to make a low-loss cavity. We chose to work with silicon which has a large refractive index (n=3.48 at 1550 nm) compared to other materials which should result in better optical confinement in a smaller mode volume and ultimately a larger g_0. Furthermore, silicon OMC nanobeams already have an optimized fabrication process which allow production of high cooperativity devices in the sideband-resolved regime [31].

3.2.1 OMC Nanobeam Design

We start with the OMC design used in previous work in our lab (detailed in [41, 49]). Of course, an optomechanical crystal cavity sitting on a lithium niobate substrate is not going to behave exactly like a suspended device, so we need to tailor the device parameters accordingly. We simulated these effects in COMSOL and the resulting optical mode is shown in Fig. 3.2. We found two main consequences of putting the optical cavity on lithium niobate. Firstly, the resonant frequencies of each mode shifts down by about 3 THz, which can be accounted for by modifying the hole-spacing parameter. We also found that waveguides optimized for suspended use became significantly undercoupled.

The other consequence is that the cavity's quality factor is degraded by about 20%. Because lithium niobate has a much higher refractive index than air, more of the mode leaks into the substrate than it would in the case of a suspended nanobeam. Integrating the absolute value of the electric field in our simulations indicates that 15% of the mode lives in the lithium niobate, compared to 2% if the same volume was made of air. We note a potentially interesting trade-off: increasing the optical losses of the cavity into the substrate

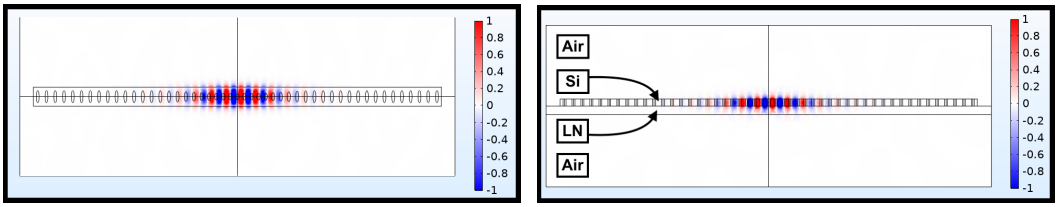

(a) *(b)*

Figure 3.2: ***Cavity Design.*** *A fundamental optical mode of a silicon cavity on $LiNbO_3$ plotted in arbitrary units. (a) Birds-eye view. (b) Cross-sectional view, with regions labeled.*

increases κ and makes it more difficult to reach the sideband resolved regime.

3.2.2 Nanofabrication Procedure

The fabrication of the silicon photonic crystal cavity nanobeams was performed in the cleanroom of the Van Leeuwenhoek Laboratory in Delft. We use electron beam lithography to define our nanobeams on an SOI chip. Then, we perform a cryogenic etch to transfer the pattern into the silicon layer. After removing the remaining resist and an inorganic chemical clean, we release the delicate structures using a vapor HF

We begin our fabrication using 5 mm by 10 mm chips diced from a six-inch Silicon-on-Insulator wafer. Our wafer was acquired from Soitec and consists of a 250 nm layer silicon on top of 3 μm thick buried silicon oxide on a silicon substrate. Our fabrication consists of four process steps, shown in Fig. 3.3.

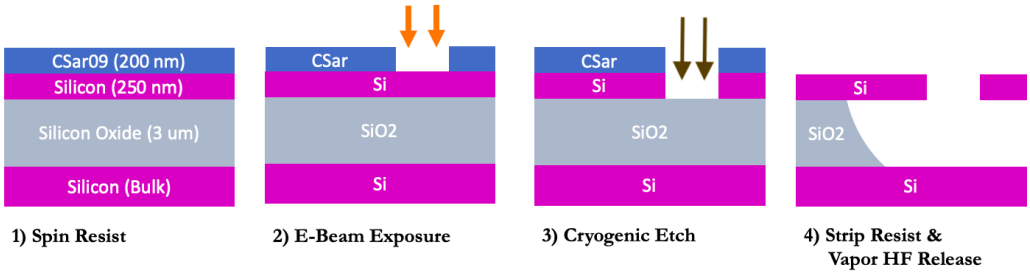

Figure 3.3: ***Fabrication Flow.*** *The steps of our fabrication process are laid out. Orange arrows in step two indicate exposure with an electron beam, while brown arrows in step three indicate reactive ion etching.*

1) Spin Resist. We spin resist CSAR-62.09 to a thickness of 200 nm on a clean SOI chip.

2) E-Beam Exposure. Then the nanobeams are patterned with an electron-beam lithography step (using a Raith 5200 Electron Beam Pattern Generator). We develop the exposed pattern by submerging in beakers of pentyl-acetate, 1:1 MIBK:IPA, and finally IPA for one minute each.

3) Cryogenic Etch. We etch the silicon in an Alcatel AMS 100 I-speeder etcher using an SF_6/O_2 chemistry at $-120°$ C. We use a cryogenic etch process to achieve nearly vertical sidewalls thanks to a sidewall passivation effect.

4) Strip Resist and Vapor HF Release. Next, we remove the resist by placing the sample in a beaker of 80° C di-methylformamide (DMF) for 5 minutes. Then we dip or devices in a Piranha solution (sulfuric acid is combined with hydrogen peroxide in a 3:1 ratio) for 7 minutes. This cleans the silicon, but some oxide forms on the surface of the nanobeams. Next, we use a Hydrofluoric Acid Vapor Etcher (HFVE) system from Idonus to release our structures. We suspect that this step also removes the surface oxides from the piranha clean. Once suspended our nanobeams are only connected to the chip by a tiny tether, so we chose to use a gentle vapor etch instead of the more common liquid HF dip. In the HFVE process our chips are placed on a holder which is heated and inverted over a pool of liquid HF. The HF evaporates and condenses on the holder, slowly etching the oxide while the silicon structure is left undisturbed. We heat the holder to 35° C and etch the chip for 60 minutes. Finally, the chips are placed on a hot plate at 80° C for one minute in order to evaporate any remaining HF. The resulting undercut radius was around 5 microns on average but could vary by ± 2 microns.

3.2.3 Optical Measurements

Next, we measured the optical reflection spectrum to gauge the performance of our cavity. Ideally, one could measure all of the nanobeams while they still suspended on the SOI donor chip and pick the best ones to slap. One should keep in mind that the frequencies of the fundamental optical modes are different when the nanobeam is surrounded by air instead of resting on lithium niobate. This became a nuisance because the 3 THz (25 nanometer) shift occasionally pushed the fundamental resonance out of range of our coupler, forcing us

to measure higher-order modes of suspended nanobeams.

However, we wanted to slap the nanobeams before investigating them in order to recreate the conditions of our transduction experiment. We placed nanobeams such that the cavity sat near the edge of a released film of lithium niobate while the coupler was suspended as shown in Fig. 3.4 (a).

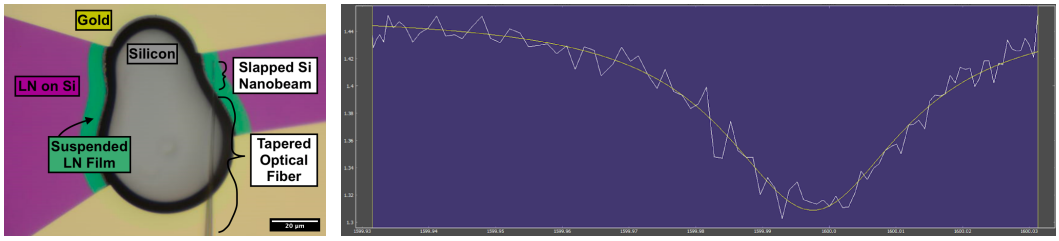

(a) *(b)*

Figure 3.4: ***Optics.*** *(a) Optical microscope image of the setup for measuring slapped nanobeams on thin film lithium niobate. (b) Reflection measurement of the fundamental mode of the optical cavity shown in (a).*

A typical optical reflection measurement consists of sweeping a tunable laser across the cavity and measuring the reflected light on a photodetector. The resulting spectra show reflection dips indicating optical resonances. Fitting a dip to a Lorentzian lineshape yields the linewidth at full width half maximum which is a measure of the rate of optical loss. The linewidth of the device shown in Fig. 3.4 was 3.8 GHz, which translates to a quality factor of 5×10^5. This linewidth is typical of the devices we measured, which usually had linewidths between 3-4 GHz. This was broader than the sub-Gigahertz linewidths seen in suspended silicon devices and indicates that we will not be in the sideband-resolved regime. We attribute the poor performance of these devices to problems with our etch recipe that resulted in poor sidewall profiles and lower optical quality factors for the nanobeams used in this work. This issue has since been resolved. However, we felt that our devices had sufficient performance for an initial proof-of-concept wavelength conversion experiment.

In addition, we noticed that our devices had shallow resonance dip depths that indicate we need to adjust our coupler design in order to transfer light in and out of our cavity with high efficiency. We assume, based on our simulations, that we are undercoupled. This could be confirmed by fabricating many devices that sweep the number of holes between the cavity

and the coupler (which changes the coupling rate) and studying the phase response [41], but we felt that the optical design of our devices could be optimized after our initial test.

3.3 Designing a Transducer

This project's short-term goal is a demonstration of room-temperature transduction in an optical cavity slapped on a piezoelectric resonator. However, as we designed our device, we had a long term goal in mind: showing efficient quantum transduction in a future, optimized device. Our planned quantum transduction scheme is a pulsed double swap operation between electro- and optomechanical devices, which imposes three strict requirements on our transducer. First, we must be able to swap an excited state of a qubit into a single phonon, which demands the highest possible electromechanical efficiency. Our conversion process must also operate with a thermal background lower than a single phonon, otherwise we will not be able to distinguish our quantum signal from classical noise. Finally, an optomechanical readout of the single phonon signal requires a optomechanical cooperativity greater than one. As we plan to expand our proof-of-concept to meet the conditions of quantum transduction, we design our device along the following guidelines.

1) Maximize Electromechanical Efficiency: ($\eta_{\mu\to m} \to 1$)

Our protocol relies on swapping a single excitation between a qubit and our mechanical resonator. This requires operation in the electromechanical strong coupling regime, where the qubit-phonon coupling rate is larger than the loss rate of the mechanical mode and the qubit decoherence rate. Recent experiments demonstrate that strong coupling in optomechanical systems is possible but practically difficult to achieve [39, 98]. In order to elude a future bottleneck, our device is designed to maximize electromechanical efficiency. Similar devices comprised of micron-scale IDTs on thin film lithium niobate have demonstrated microwave to mechanical coupling efficiency $\eta_{\mu\to m} = 50\%$ [22].

2) Ground State Mechanics: ($n_{added} < 1$)

In addition to being efficient, our linear transduction process must add less noise than the input signal intensity. In the case of our scheme, where the input signal consists of a single microwave photon, this necessitates that the converter must operate close to its quantum motional ground state, with a thermal occupation less than one [99].

$$n_{th} = \frac{e^{-k_B T/\hbar\Omega_m}}{1 - e^{-k_B T/\hbar\Omega_m}} < 1 \tag{3.12}$$

We will be able to cryogenically initialize our mechanical resonator close to its ground state because we will operate our transducer in a dilution fridge at millikelvin temperatures where $\hbar\Omega_m > k_B T$. When we cool our device in the dilution refrigerator we can confirm this using sideband asymmetry to measure the thermal occupation of the resonator. In addition, heating due to absorption of the optical and the RF drive tones will add noise to the output signal. Typically this leads to a trade-off between transduction efficiency and added noise in mechanical resonators at the quantum limit [100]. We believe this added noise can be kept under a single phonon, as recent experiments which similarly use IDTs to excite a mechanical mode of a nanobeam have demonstrated that piezo-optomechanical conversion with acceptable added noise can be achieved by operation in the mechanical ground state [24, 39]. The added noise will be investigated using a Hanbury-Brown-Twiss type measurement of converted optical photons, following the procedure in Ref. [24].

We should note that the flexibility of our pick-and-place fabrication is especially useful here. If we find that we are limited by optical absorption, we can change the material of our optical cavity with only minor modifications to our design. Likewise, if we find that we require a more isolated or more thermalized mechanical resonator, we can change the lithium niobate structure while leaving the optical cavity unaltered. In Section 2.2, we mentioned that we can design the mechanical supermode. This is the point in our research where we will need to optimize our resonator.

3) Finally, Refine Optics: ($C_{om} = \frac{4g_{om}^2}{\kappa_o \gamma_m} > 1$)

Once a qubit excitation has been efficiently converted to a phonon with subphoton added noise, that phonon must be detected optically. We can use the optomechanical beam-splitter interaction (Eq. 3.9) to swap gigahertz phonons and telecom photons as long as the condition $C_{om} = \frac{4g_{om}^2}{\kappa_o \gamma_m} > 1$ is met [45]. This is a relatively stringent requirement compared to the other two because the optomechanical coupling rate is parametrically enhanced by the intracavity photon number as $g_{om} = g_0\sqrt{n_{cav}}$.

We expect that our transducer will have a lower single photon optomechanical coupling rate than other silicon OMC nanobeam devices [47] given the relation $g_0 \propto \frac{1}{m_{eff}}$ because the effective mass of our mechanical resonator is large in comparison [30]. We view this as a trade-off, because the large area of our resonator is designed to maximize electromechanical

efficiency. We also feel like the optical and mechanical loss rates κ_o, γ_m can be improved further than the values reported in this work. The optical losses can be mitigated by optimizing the design of the photonic crystal and cleaner fabrication of the silicon nanobeams. Furthermore, larger optical coupling efficiencies can be achieved by modifying the waveguide and coupler to achieve critical coupling. Finally, we expect that cooling the device in a dilution refrigerator will result in lower mechanical losses. By mitigating losses and optimizing our design, we feel confident that a future device can reach the high optomechanical cooperativity regime.

3.3.1 Simulating the Optomechanical Coupling Rate

The last step of our resonator design is understanding the optomechanical properties of our hybrid silicon nanobeam-lithium niobate electromechanical resonator system. We used COMSOL to simulate the optical and mechanical modes of the structure, shown in Fig. 3.5. This figure shows the fundamental TE-like mode of a silicon photonic crystal nanobeam placed on a $15 \times 5.5 \times .3\ \mu m$ X-cut lithium niobate thin film BAW resonator as well as the strain and displacement fields of the mechanical supermode of the nanobeam-on-resonator device. We find mechanical modes that match the profiles of the 7th, 8th, and 9th longitudinal order asymmetric lamb wave modes at 1.55, 1.87, and 2.16 GHz. Furthermore, the difference between these modes gives us an estimate of the FSR of $\approx$ 300 MHz, which approximately matches the expected phase velocity of an A0 lamb wave. Finally, we simulated the admittance of the 4-finger IDT in in Fig. 3.5, which yielded a electromechanical coupling coefficient $k^2 \approx 1\%$. This result is consistent with what we reported in similar simulations of the A0 mode.

We also used our simulation to calculate the single-photon optomechanical coupling rate of our device using the method described in Ref. [42]. We found $g_0 \approx 50$ kHz between the fundamental TE-like mode and lamb wave-type supermode at 1.55 GHz. The results of these simulations are to be taken with a grain of salt, as the pick-and-place fabrication we chose to use makes this system difficult to model precisely. However, this calculation can help us gauge how robust our device is to imprecision in our slapping process. We simulated a wide range of placements of the nanobeam on the resonator by shifting the location of the nanobeam on the resonator in the y and z directions indicated in Fig. 3.5. We found that

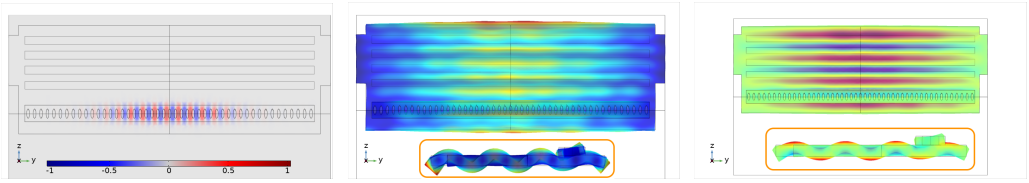

(a) (b) (c)

Figure 3.5: ***COMSOL Modeling.*** *Results of a simulated optomechanical transduction device. The silicon nanobeam sits on the thin film lithium niobate resonator, viewed from the top. (a,b) Displacement and dominant strain field of a piezomechanical supermode at 1.551 GHz. Side view shown in orange insets. (c) Electric field of the fundamental mode of the optical nanocavity at 1580 nm.*

the g_0 was most sensitive to mispositioning in the y direction. However, the g_0 did not drop by more than 10% for misplacements under 150 nanometers, a value within our placement imprecision tolerance. We also looked at what happens if the nanobeam is slightly rotated with respect to the thin film resonator, and we found that g_0 seems to be robust to rotations of $\pm 4°$, much larger than we anticipate based on our work in Chapter 1.

3.4 Transduction Measurement

We implement a wavelength converter with photonic crystal cavity nanobeam slapped on top of a piezoelectric resonator at room temperature. A microwave tone swept over the device will excite a hybrid nanobeam/piezoelectric mechanical supermode on resonance. At the same time, laser light is continuously pumped optical into the nanobeam. detuned to the blue side of the cavity by the mechanical frequency. On resonance, the mechanical motion excited by the microwave signal will drive the stokes process described by Eq. 3.8 and create sidebands on the laser drive tone at the cavity frequency. The optical intensity resulting from the beat note between the reflected cavity and pump photons can be measured by monitoring the light reflected from the cavity on a fast photodiode. Key parameters such as optomechanical coupling g_0 and microwave to optical efficiency η_{eo} can be extracted by comparing the response of the output of the fast photodetector to the microwave input with a VNA. Appendix A shows this analysis in full.

We report our most successful piezo-optomechanical transduction measurement. All measurements shown in this section were taken using the device shown in Fig. 3.6. This device was a $15 \times 5.5 \times .3$ μm X-cut lithium niobate thin film BAW resonator fabricated using the procedure laid out in Section 2.2. It was fabricated with two thick and two thin tethers - a four finger IDT is patterned through the thick tethers and the thin tethers are designed to support a slapped silicon OMC such that the coupler is suspended but the cavity is in slapped firmly onto the center of the mechanical resonator. The IDT has only two finger pairs for two reasons. We aimed to reduce the effective mass of the supermode, thereby increasing g_0 at the expense of k^2. In this proof-of-concept experiment, we felt comfortable making this trade-off because we wanted to get an idea of the maximum optomechanical performance of slapped devices. However, in a future quantum transduction experiment we want the k^2 to be as high as possible.

The techniques laid out in Section 1.2 were used to align and slap the silicon nanobeam. We set out to measure the microwave to optical conversion efficiency at room temperature as well as the half-wave voltage (V_π) of our transducer, but unfortunately the device was destroyed after the former measurement. We aren't sure exactly what went wrong, but after some hours of measurement the microwave drive stopped working and nothing more could be measured.

3.4.1 Characterization of the Conversion Device

Before a transmission measurement was conducted, we measured the microwave and optical reflection spectra to characterize our device. The results are shown in Fig. 3.7. Two prominent dips in the microwave reflection spectrum indicate mechanical resonances at 1.411 and 2.013 GHz with loaded quality factors of 283 and 251, respectively. We see smaller dips around 1.1, 1.7, and 2.4 GHz, so see a dip approximately every 300 MHz. We can conjecture that we are coupling to a A0-type mode which is predicted to have a similar FSR. The low mechanical quality factor of this device can be partially attributed to the fact that this measurement was conducted five weeks after the device was fabricated. Earlier measurements on the device show quality factors above 1000 before the nanobeam was slapped and over 500 afterwards, indicating some degradation in our devices over time.

Optical spectroscopy is performed using a Santec TSL-550 tunable diode laser. The re-

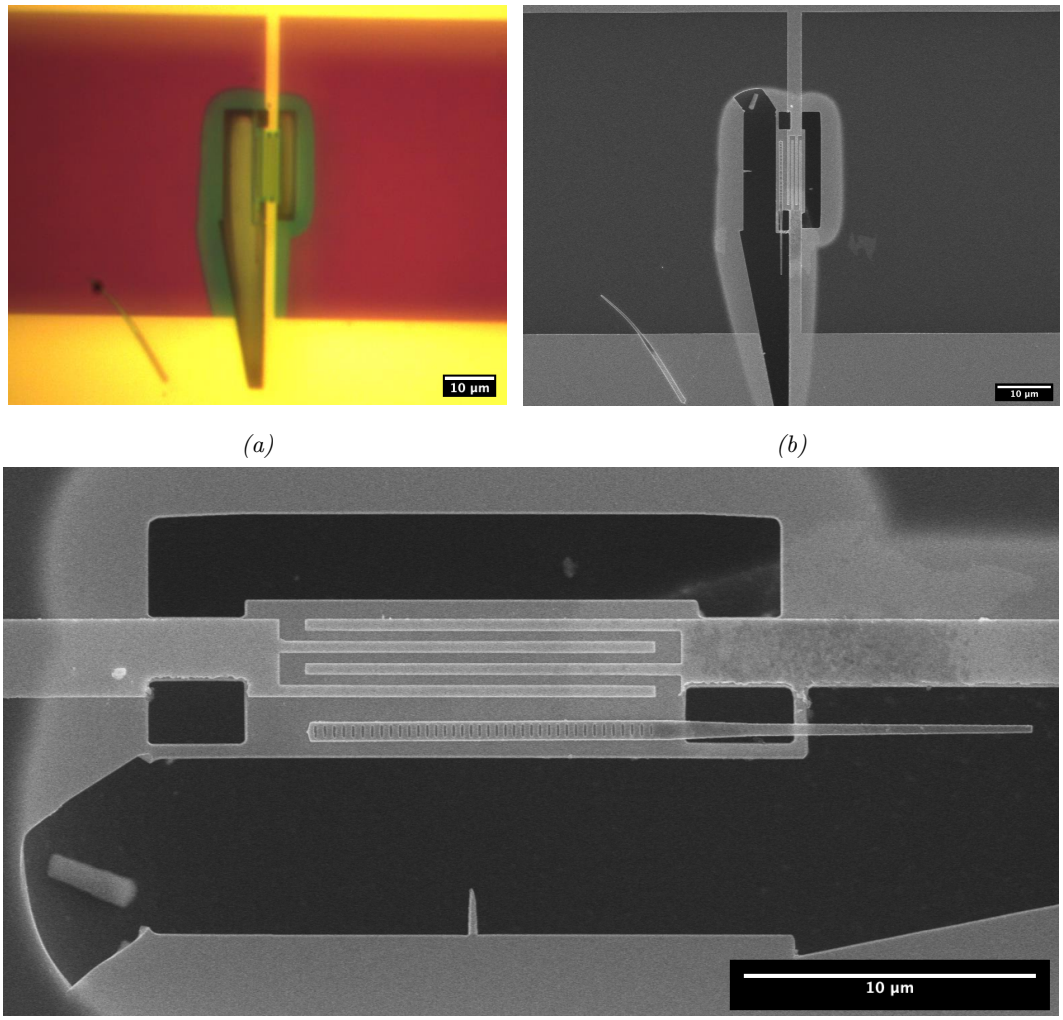

(a) *(b)*

(c)

Figure 3.6: ***Final Device.*** *Images of the device used for the measurements in this section. (a) Optical image of the device before the results reported in this section were measured. (b,c) SEM images of the device after the measurement. Some damage to the device is visible.*

flection spectrum of the device shows two prominent resonances at 1588 and 1617 nanometers. We suspect that the 1588 nm mode we used is the second harmonic instead of the fundamental optical mode. Finer scans around the modes shows evidence of a third resonance at 1565 nm, but it was too weakly coupled to use in this experiment. The larger

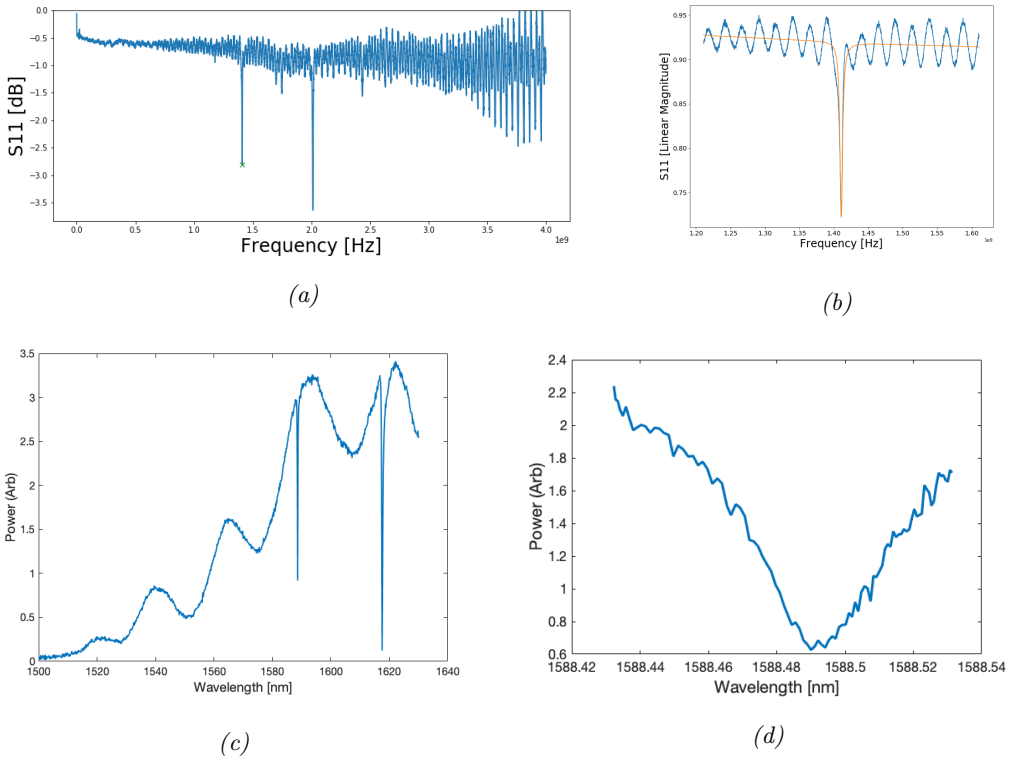

Figure 3.7: ***Characterization of the Conversion Device.*** *(a) Microwave reflection spectrum with the resonance at 1.411 GHz indicated. (b) Fitted resonance at 1.411 GHz. (c) Optical reflection spectrum (d) Fine scan of the optical resonance at 1588 nm.*

optical linewidth of 6.61 GHz and distance from the intended center frequency of 1550 nm serves as further confirmation. In future work, the coupler and input waveguide will need to be re-designed in order to access the fundamental optical mode. We proceeded to measure this device despite these non-ideal conditions. We note that our device operates in the near sideband-resolved regime.

3.4.2 Transduction Results

Finally, we measure microwave to optical transduction with our device. In order to perform this measurement, we set up our RF probe and optical fiber so that both could be seen at the same time under an optical microscope, as shown in Fig. 3.8 (a). We found

that touching down the RF probe could move the chip, and thus had to carefully position both the RF probe and fiber just above the chip, touch down with the probe, and finally align the tapered fiber. However, the setup was sensitive to air currents in the room which presents difficulties in our measurement if the optical fiber drifts by more than a hundred nanometers.

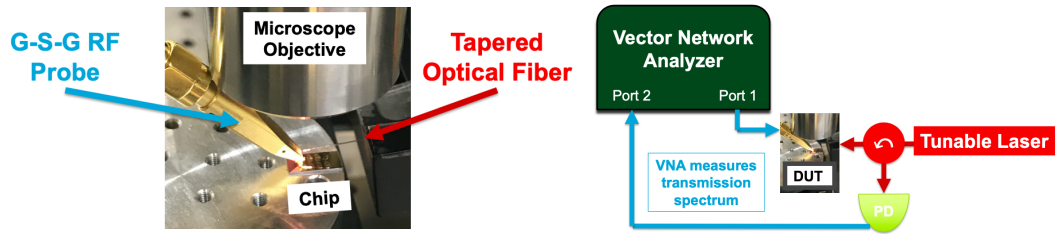

(a) *(b)*

Figure 3.8: ***Measurement Setup.*** *(a) The configuration used for simultaneously probing the optical and RF responses of our device. (b) Diagram of our transmission measurement.*

Wavelength conversion was perform as depicted in Fig. 3.8 (b): Port 1 of the VNA (Rohde and Schwarz ZNB-40) was connected to the G-S-G RF probe and calibrated open. The probe was then put in contact with the chip in order to drive the IDTs. Simultaneously, light from a tunable laser passes through a Variable Optical Attenuator (VOA) and polarization controller before entering into one port of a circulator. The output is connected to a tapered optical fiber which is aligned to the coupler of the slapped silicon optomechanical crystal cavity. Reflected light passes back through the circulator and is directed onto a fast photodiode (ET-3500AF) with a calibrated responsibility of $R_{PD} = 1300V/W$. Finally, the output of the photodiode is connected to Port 2 the VNA.

We select the highest Q mode at 1.411 GHz as our mechanical resonance, and lock the laser detuned to the blue side of the optical resonance by the mechanical frequency $\omega_d = \omega_c + \Omega_m$. At room temperature and high optical power the mechanical resonance generates sidebands on the optical drive tone, so we could just as easily have locked to the red side of the optical cavity. We adjust the polarization filters and VOA and measure the input intensity sent into the cavity through the tapered fiber to be $I_{In} = 25.3\mu W$. Meanwhile, we drive the IDT with a continuous microwave tone of $-30dB$ at 1.411 GHz from Port 1 of the VNA. The reflected optical light passes through a circulator the fast photodiode,

which measures the RF beat note between converted cavity photons and reflected drive photons. The received optical power at the photodiode was measured to be $I_{Rec}804nW$. The output of the fast photodetector is sent to Port 2 of the VNA, so a S_{21} scan yields a transmission-type measurement of microwave to optical transduction. The data are shown in Fig. 3.9.

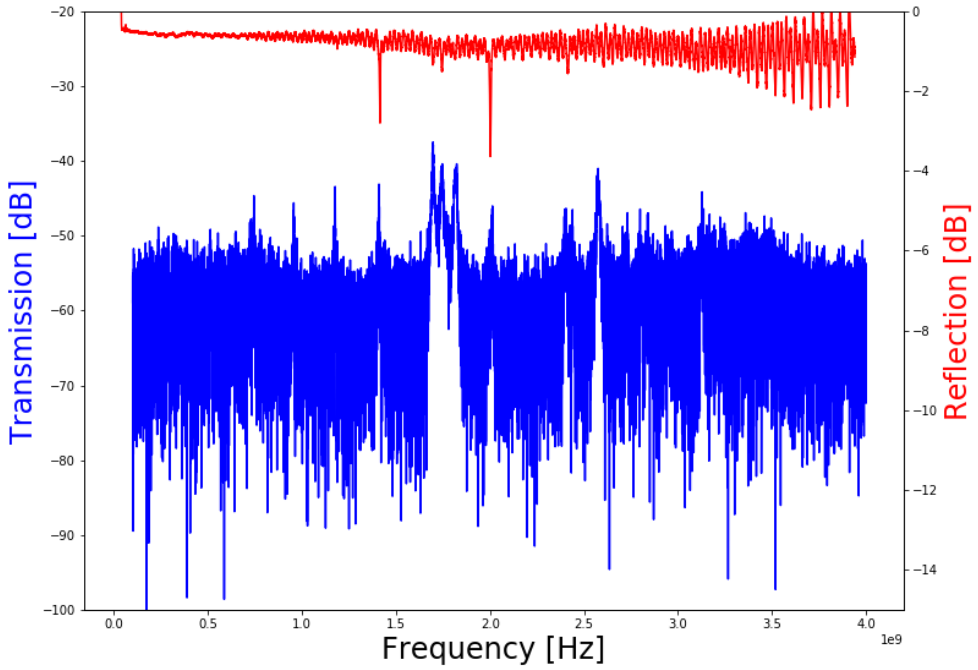

Figure 3.9: ***Transduction.*** *S_{21} and S_{11} traces are shown in blue and red, respectively. Microwave input power was set to -30 dB while optical input power was 25 μW.*

We measure a peak in the S_{21} near 1.4 GHz with peak amplitude -42.5 dB. Note that the maximum signal is -36 dB, received around 1.7 GHz, which corresponds to very lossy mechanical modes. Future work will investigate these modes, but for now we continue to focus on transduction through the 1.411 GHz mode. The single-photon optomechanical coupling rate g_0 can be extracted from the S_{21} by

$$S_{21} \approx \frac{8g_0^2\gamma_e\kappa_e^2R_{PD}^2I_{Rec}^2}{\hbar\gamma^2\Omega_m^3\kappa^2R_{Load}} \tag{3.13}$$

in the near-sideband resolved regime where $R_{Load} = 50\Omega$ is the impedance of the VNA ports. This calculation follows Ref. [22] and the full derivation can be found in Appendix A of this work.

The microwave to optical transduction efficiency $\eta_{\mu\to o}$ is the product of the single photon cooperativity (C_0), the intracavity photon number (n_{cav}), and the microwave and optical external coupling efficiencies ($\eta_{ext,\mu}, \eta_{ext,o}$, respectively):

$$\eta_{\mu\to o} = \frac{4g_0^2}{\gamma\kappa} \cdot \frac{\kappa_e I_{In}}{\Omega_m^2 \hbar\omega_c} \cdot \frac{2\gamma_e}{\gamma} \cdot \frac{2\kappa_e}{\kappa} = C_0 \cdot n_{cav} \cdot \eta_{ext,\mu} \cdot \eta_{ext,o} \tag{3.14}$$

Our results are reported in Table 3.1. We find $g_0 = 5.1$ kHz and $g_{om} = g_0\sqrt{n_{cav}} = 1.2$ MHz. Large loss rates of the optical and mechanical resonators of 6.6 GHz and 5.2 MHz keep this device out of the $C_{om} > 1$ regime. The relatively high external coupling efficiencies result in a photon number conversion efficiency of $\eta_{\mu\to o} = 6.111 \times 10^{-6}$ at an optical power of $I_{In} = 25\mu W$.

Parameter	Value
$\omega_c/2\pi$	1.889 THz
$\Omega_m/2\pi$	1.41 GHz
$\gamma/2\pi$	5.2 MHz
$2\gamma_e/\gamma$	.20
$\kappa/2\pi$	6.61 GHz
$2\kappa_e/\kappa$	.16
R_{PD}	1300 V/W
I_{Rec}	804 nW
R_{Load}	50 Ω
S_{21}	−42.5 dB
g_0	5.106 kHz
C_0	3.165×10^{-9}
n_{cav}	54977
$\eta_{\mu\to o}$	6.111×10^{-6}

Table 3.1: ***Experimental Values***

3.4.3 Analysis and Future Improvements

We feel that this result successfully demonstrates that microwave to optical is possible using our hybrid silicon on lithium niobate device. These measurements were a proof of concept, but our analysis leaves us hopeful that this approach can produce state of the art devices. The large electromechanical efficiency of 20%, made possible by our choice to use thin film lithium niobate, is a particularly encouraging figure. However, the measured g_0 was an order of magnitude lower than our simulated value of 50 kHz, resulting in a lower C_0 than we would have liked. We feel like there are some additional adjustments to this device that can be made fairly easily that would boost the figures of merit by several orders of magnitude. Several of them are listed below:

- One critical improvement is design waveguides and couplers that allow access to the fundamental optical mode. The photonic crystal cavity was designed to optimize the fundamental mode, and as a result we measured increased losses in the device we used. The second harmonic also lowers the mode overlap between optical and mechanical modes which decreases g_0. Additional improvements to the cleanliness of the fabrication process will also hopefully yield sub-gigahertz linewidth optical resonances.

- Our results suggest that we are not using the best possible mechanical mode. Based on the FSR and electromechanical coupling efficiency of our simulations and measurements, we think we are actuating an A0-like supermode of the nanobeam and mechanical resonator. Our work in Chapter 2 leads us to believe that an S0 or SH0 type mode would have a larger k^2 and thus stronger transduction properties. Our measurement (Fig. 3.9) shows more transmission through a series of modes around 1.7 GHz which barely appear in the reflection spectrum than through our selected mode at 1.4 GHz - further investigation should help us understand which modes these are and how we can take advantage of them.

- There are other ways we can improve the design mechanical resonator. Moving our devices to higher frequencies and finding ways to focus our acoustic resonances should lead to significant decreases in effective mass. Replacing our tethers with a phononic shield should help to isolate our device from noise and drastically increase the mechanical quality factors of modes within a bandgap. Finally, further simulations and mea-

surements can further explore which acoustic direction of propagations and nanobeam placements optimized our supermode.

- Perhaps the easiest improvement to make is preventing device degradation by measuring as soon as possible. This should increase our yield and produce devices with higher mechanical quality factors.

- Finally, we note that this measurement was difficult to make. We measured two dozen devices and only recorded one decent transmission measurement. While that was partially due to the inexperience of the author, our devices were not easy to measure multiple times, as it was very easy to 'unslap' the nanobeams during measurement. We advise experimenters to couple to the nanobeam using a lensed fiber to avoid these issues in the future.

Conclusion

This project began by identifying two major weaknesses of nanobeam-based piezo-optomechanical transducers: that monolithic designs require sacrifices between good opto- and electromechanical materials and that the electromechanical efficiency is often sacrificed for large optomechanical cooperativity. In Chapter 1, we develop a technique for assembly of novel, hybrid-material devices. Next, we introduce thin film lithium niobate BAW resonators designed for optomechanical transduction in Chapter 2. In the final chapter, we combine these resonators with silicon OMC nanobeams using our slapping technique to demonstrate a proof of concept wavelength conversion experiment. This research is an exciting new addition to the list of attempts at quantum microwave to optical transduction. Further work developing these devices would provide insight into how far slapping can go as an experimental methodology.

Hybrid $LiNbO_3$-on-Silicon Architectures

The author is also excited about studying other structures assembled by slapping. We briefly share the preliminary results of two side-projects which use the reverse approach of that used in this work - slapping lithium niobate onto silicon. This is of interest because silicon optomechanical crystal nanobeams are well understood devices that make use of widely understood fabrication techniques resulting in state-of-the-art devices with the added benefit of integrability in photonic circuits. Furthermore, studies have shown that silicon can be a platform for high-performance transmon qubits (which lithium niobate is not) [101]. Therefore, it may make sense to use slapping to integrate small lithium niobate acoustic resonators with silicon OMCs on an SOI chip.

We show what such a device could look like in Fig. 3.10, which shows a $5\mu\text{m} \times 600\text{nm} \times$

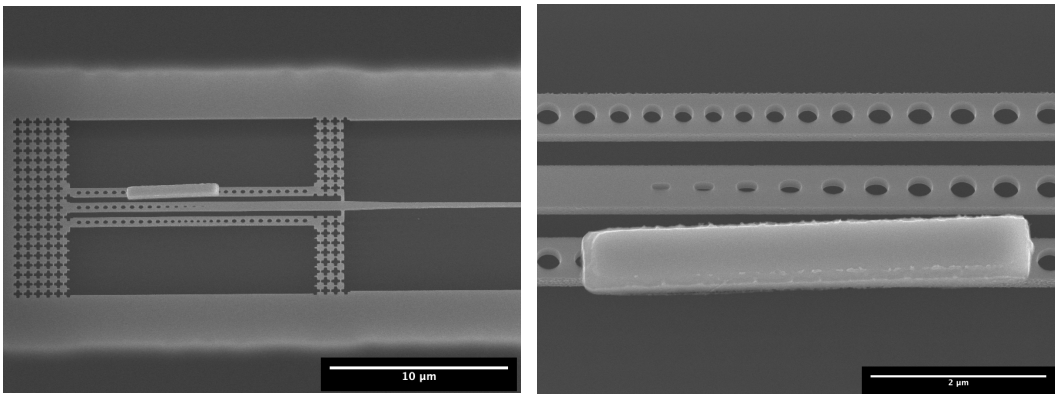

(a) *(b)*

Figure 3.10: ***Slapping on Silicon Nanobeams.*** *(a) Birds-eye view of a lithium niobate-on-silicon nanobeam device. (b) Close-up image of the slapped lithium niobate string.*

300nm lithium niobate string slapped on top of a silicon nanobeam. This test confirmed that our slapping precision is good enough to place a small string onto a thin nanobeam and that the nanobeams can survive the slapping procedure without collapsing. However, the lithium niobate shifted the optical resonances too far away to be measured with the frequency range of the available lasers. Further investigation is required to determine how the optical and mechanical resonances of these devices are affected. The author notes that the slapping procedure was not more difficult than that described in Chapter 1, as we created this device on our first attempt. The downsides of this strategy are the loss of some design freedom over the acoustic supermode, and it may be difficult to efficiently actuate acoustic modes in the lithium niobate.

An alternative strategy is to suspend a lithium niobate slab on an SOI chip. Electrodes could be used to excite acoustic modes in the lithium niobate and a phononic waveguide could transfer excitations to the silicon nanobeam. One way to create such a waveguide is with a defect in a phononic shield, an architecture that should also encourage very large mechanical quality factors. An aluminum nitride on silicon device with a similar architecture recently demonstrated efficient microwave to optical conversion in Ref. [39].

Our early attempt to design and fabricate the electromechanical element of these structures is shown in Fig. 3.11. We conclude that lithium niobate strings can be accurately suspended over a slot in an SOI substrate surrounded by a phononic shield, but no mea-

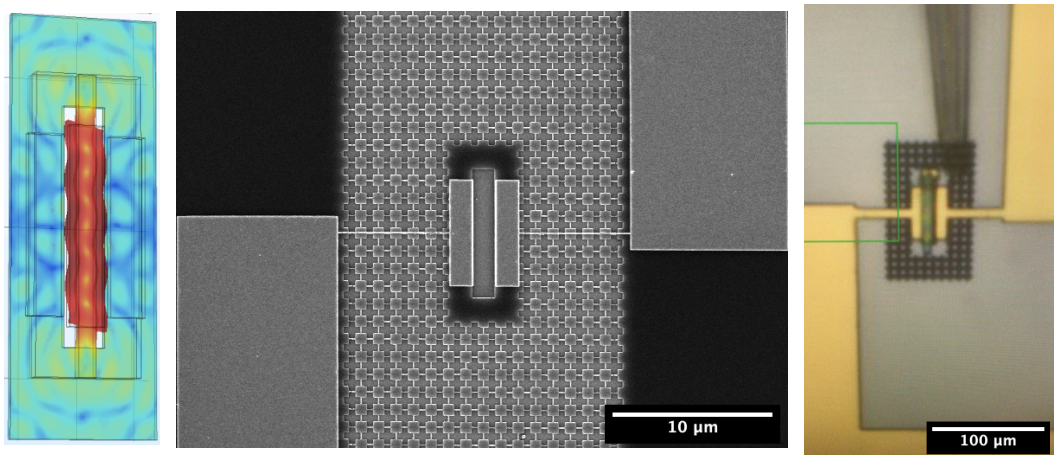

(a) *(b)* *(c)*

Figure 3.11: ***Lithium Niobate on SOI Electromechanics.*** *(a) COMSOL simulation of the displacement of a 1.8 GHz shear mode of an lithium niobate string suspended over an SOI substrate. (b) SEM of a SOI phononic shield with gold electrodes patterned on top. The lithium niobate string will be slapped over the central slot etched into the silicon. (c) Optical microscope image of such a slapped string.*

surements have been performed yet due to the COVID-19 pandemic. Further experiments will have to be conducted to understand the utility of these devices.

Bibliography

[1] H Jeff Kimble. The quantum internet. *Nature*, 453(7198):1023–1030, 2008.

[2] Frédéric Grosshans, Gilles Van Assche, Jérôme Wenger, Rosa Brouri, Nicolas J Cerf, and Philippe Grangier. Quantum key distribution using gaussian-modulated coherent states. *Nature*, 421(6920):238–241, 2003.

[3] Stefano Pirandola, Bhaskar Roy Bardhan, Tobias Gehring, Christian Weedbrook, and Seth Lloyd. Advances in photonic quantum sensing. *Nature Photonics*, 12(12):724–733, 2018.

[4] Robert Beals, Stephen Brierley, Oliver Gray, Aram W Harrow, Samuel Kutin, Noah Linden, Dan Shepherd, and Mark Stather. Efficient distributed quantum computing. *Proceedings of the Royal Society A: Mathematical, Physical and Engineering Sciences*, 469(2153):20120686, 2013.

[5] John Preskill. Quantum computing in the nisq era and beyond. *Quantum*, 2:79, 2018.

[6] Michel H Devoret and Robert J Schoelkopf. Superconducting circuits for quantum information: an outlook. *Science*, 339(6124):1169–1174, 2013.

[7] Göran Wendin. Quantum information processing with superconducting circuits: a review. *Reports on Progress in Physics*, 80(10):106001, 2017.

[8] Stephanie Wehner, David Elkouss, and Ronald Hanson. Quantum internet: A vision for the road ahead. *Science*, 362(6412):eaam9288, 2018.

[9] David P DiVincenzo. The physical implementation of quantum computation. *Fortschritte der Physik: Progress of Physics*, 48(9-11):771–783, 2000.

[10] Gershon Kurizki, Patrice Bertet, Yuimaru Kubo, Klaus Mølmer, David Petrosyan, Peter Rabl, and Jörg Schmiedmayer. Quantum technologies with hybrid systems. *Proceedings of the National Academy of Sciences*, 112(13):3866–3873, 2015.

[11] Nicholas J Lambert, Alfredo Rueda, Florian Sedlmeir, and Harald GL Schwefel. Coherent conversion between microwave and optical photons—an overview of physical implementations. *Advanced Quantum Technologies*, page 1900077, 2019.

[12] Nikolai Lauk, Neil Sinclair, Shabir Barzanjeh, Jacob P Covey, Mark Saffman, Maria Spiropulu, and Christoph Simon. Perspectives on quantum transduction. *Quantum Science and Technology*, 5(2):020501, 2020.

[13] David AB Miller. Attojoule optoelectronics for low-energy information processing and communications. *Journal of Lightwave Technology*, 35(3):346–396, 2017.

[14] AS Zibrov, AB Matsko, O Kocharovskaya, YV Rostovtsev, GR Welch, and MO Scully. Transporting and time reversing light via atomic coherence. *Physical review letters*, 88(10):103601, 2002.

[15] Shankar G Menon, Kevin Singh, Johannes Borregaard, and Hannes Bernien. Nanophotonic quantum network node with neutral atoms and an integrated telecom interface. *arXiv preprint arXiv:2002.05175*, 2020.

[16] Lin Tian and Hailin Wang. Optical wavelength conversion of quantum states with optomechanics. *Physical Review A*, 82(5):053806, 2010.

[17] Lin Tian. Optoelectromechanical transducer: Reversible conversion between microwave and optical photons. *Annalen der Physik*, 527(1-2):1–14, 2015.

[18] Joerg Bochmann, Amit Vainsencher, David D Awschalom, and Andrew N Cleland. Nanomechanical coupling between microwave and optical photons. *Nature Physics*, 9(11):712–716, 2013.

[19] Tolga Bagci, Anders Simonsen, Silvan Schmid, Luis G Villanueva, Emil Zeuthen, Jürgen Appel, Jacob M Taylor, A Sørensen, Koji Usami, Albert Schliesser, et al. Optical detection of radio waves through a nanomechanical transducer. *Nature*, 507(7490):81–85, 2014.

[20] Krishna C Balram, Marcelo I Davanço, Jin Dong Song, and Kartik Srinivasan. Coherent coupling between radiofrequency, optical and acoustic waves in piezo-optomechanical circuits. *Nature photonics*, 10(5):346, 2016.

[21] Andrew P Higginbotham, PS Burns, MD Urmey, RW Peterson, NS Kampel, BM Brubaker, Graeme Smith, KW Lehnert, and CA Regal. Harnessing electro-optic correlations in an efficient mechanical converter. *Nature Physics*, 14(10):1038–1042, 2018.

[22] Linbo Shao, Mengjie Yu, Smarak Maity, Neil Sinclair, Lu Zheng, Cleaven Chia, Amirhassan Shams-Ansari, Cheng Wang, Mian Zhang, Keji Lai, et al. Microwave-to-optical conversion using lithium niobate thin-film acoustic resonators. *Optica*, 6(12):1498–1505, 2019.

[23] Wentao Jiang, Christopher J. Sarabalis, Yanni D. Dahmani, Rishi N. Patel, Felix M. Mayor, Timothy P. McKenna, Raphaël Van Laer, and Amir H. Safavi-Naeini. Efficient bidirectional piezo-optomechanical transduction between microwave and optical frequency. sep 2019.

[24] Moritz Forsch, Robert Stockill, Andreas Wallucks, Igor Marinković, Claus Gärtner, Richard A Norte, Frank van Otten, Andrea Fiore, Kartik Srinivasan, and Simon Gröblacher. Microwave-to-optics conversion using a mechanical oscillator in its quantum ground state. *Nature Physics*, 16(1):69–74, 2020.

[25] Xu Han, Wei Fu, Changchun Zhong, Chang-Ling Zou, Yuntao Xu, Ayed Al Sayem, Mingrui Xu, Sihao Wang, Risheng Cheng, Liang Jiang, et al. 10-ghz superconducting cavity piezo-optomechanics for microwave-optical photon conversion. *arXiv preprint arXiv:2001.09483*, 2020.

[26] G Arnold, M Wulf, S Barzanjeh, ES Redchenko, A Rueda, WJ Hease, F Hassani, and JM Fink. Converting microwave and telecom photons with a silicon photonic nanomechanical interface. *arXiv preprint arXiv:2002.11628*, 2020.

[27] Yiwen Chu, Prashanta Kharel, William H Renninger, Luke D Burkhart, Luigi Frunzio, Peter T Rakich, and Robert J Schoelkopf. Quantum acoustics with superconducting qubits. *Science*, 358(6360):199–202, 2017.

[28] Kevin Joseph Satzinger, YP Zhong, H-S Chang, Gregory A Peairs, Audrey Bienfait, Ming-Han Chou, AY Cleland, Cristopher R Conner, Étienne Dumur, Joel Grebel, et al. Quantum control of surface acoustic-wave phonons. *Nature*, 563(7733):661–665, 2018.

[29] Patricio Arrangoiz-Arriola, E. Alex Wollack, Zhaoyou Wang, Marek Pechal, Wentao Jiang, Timothy P. McKenna, Jeremy D. Witmer, Raphaël Van Laer, and Amir H. Safavi-Naeini. Resolving the energy levels of a nanomechanical oscillator, jul 2019.

[30] Markus Aspelmeyer, Tobias J Kippenberg, and Florian Marquardt. Cavity optomechanics. *Reviews of Modern Physics*, 86(4):1391, 2014.

[31] Jasper Chan, Amir H. Safavi-Naeini, Jeff T. Hill, Seán Meenehan, and Oskar Painter. Optimized optomechanical crystal cavity with acoustic radiation shield. *Applied Physics Letters*, 101(8):081115, aug 2012.

[32] Jasper Chan, TP Mayer Alegre, Amir H Safavi-Naeini, Jeff T Hill, Alex Krause, Simon Gröblacher, Markus Aspelmeyer, and Oskar Painter. Laser cooling of a nanomechanical oscillator into its quantum ground state. *Nature*, 478(7367):89–92, 2011.

[33] Ralf Riedinger, Sungkun Hong, Richard A Norte, Joshua A Slater, Juying Shang, Alexander G Krause, Vikas Anant, Markus Aspelmeyer, and Simon Gröblacher. Nonclassical correlations between single photons and phonons from a mechanical oscillator. *Nature*, 530(7590):313–316, 2016.

[34] Yinan Zhang, Murray W McCutcheon, Ian B Burgess, and Marko Loncar. Ultra-high-q te/tm dual-polarized photonic crystal nanocavities. *Optics letters*, 34(17):2694–2696, 2009.

[35] Wentao Jiang, Rishi N. Patel, Felix M. Mayor, Timothy P. McKenna, Patricio Arrangoiz-Arriola, Christopher J. Sarabalis, Jeremy D. Witmer, Raphaël Van Laer, and Amir H. Safavi-Naeini. Lithium niobate piezo-optomechanical crystals. *Optica*, 6(7):845, jul 2019.

[36] Robert Stockill, Moritz Forsch, Grégoire Beaudoin, Konstantinos Pantzas, Isabelle Sagnes, Rémy Braive, and Simon Gröblacher. Gallium phosphide as a piezoelectric platform for quantum optomechanics. *Physical review letters*, 123(16):163602, 2019.

[37] Katharina Schneider, Yannick Baumgartner, Simon Hönl, Pol Welter, Herwig Hahn, Dalziel J Wilson, Lukas Czornomaz, and Paul Seidler. Optomechanics with one-dimensional gallium phosphide photonic crystal cavities. *Optica*, 6(5):577–584, 2019.

[38] Marcelo Wu, Emil Zeuthen, Krishna Coimbatore Balram, and Kartik Srinivasan. Microwave-to-optical transduction using a mechanical supermode for coupling piezoelectric and optomechanical resonators. *Phys. Rev. Applied*, 13:014027, Jan 2020.

[39] Mohammad Mirhosseini, Alp Sipahigil, Mahmoud Kalaee, and Oskar Painter. Quantum transduction of optical photons from a superconducting qubit, 2020.

[40] Amnon Yariv and Pochi Yeh. *Optical waves in crystals*, volume 5. Wiley New York, 1984.

[41] Igor Marinković. *Optomechanical Devices in the Quantum Regime*. PhD thesis, Delft University of Technology, 2019.

[42] Jasper Chan. *Laser cooling of an optomechanical crystal resonator to its quantum ground state of motion*. PhD thesis, California Institute of Technology, 2012.

[43] Amir H Safavi-Naeini. *Quantum optomechanics with silicon nanostructures*. PhD thesis, California Institute of Technology, 2013.

[44] A H Safavi-Naeini, T P Mayer Alegre, J Chan, M Eichenfield, M Winger, Q Lin, J T Hill, D E Chang, and & O Painter. Electromagnetically induced transparency and slow light with optomechanics. *Nature*, 2011.

[45] Jeff T Hill, Amir H Safavi-Naeini, Jasper Chan, and Oskar Painter. Coherent optical wavelength conversion via cavity optomechanics. *Nature communications*, 3(1):1–7, 2012.

[46] Sungkun Hong, Ralf Riedinger, Igor Marinković, Andreas Wallucks, Sebastian G Hofer, Richard A Norte, Markus Aspelmeyer, and Simon Gröblacher. Hanbury brown and twiss interferometry of single phonons from an optomechanical resonator. *Science*, 358(6360):203–206, 2017.

[47] Ralf Riedinger, Andreas Wallucks, Igor Marinković, Clemens Löschnauer, Markus Aspelmeyer, Sungkun Hong, and Simon Gröblacher. Remote quantum entanglement between two micromechanical oscillators. *Nature*, 556(7702):473–477, 2018.

[48] Igor Marinković, Andreas Wallucks, Ralf Riedinger, Sungkun Hong, Markus Aspelmeyer, and Simon Gröblacher. Optomechanical bell test. *Physical review letters*, 121(22):220404, 2018.

[49] Andreas Wallucks. *Towards an Optomechanical Quantum Memory: Preparation and Storage of Non-Classical States in High-Frequency Mechanical Resonators*. PhD thesis, Delft University of Technology, 2020.

[50] Simon Gröblacher, Jeff T Hill, Amir H Safavi-Naeini, Jasper Chan, and Oskar Painter. Highly efficient coupling from an optical fiber to a nanoscale silicon optomechanical cavity. *Applied Physics Letters*, 103(18):181104, 2013.

[51] TG Tiecke, KP Nayak, Jeffrey Douglas Thompson, T Peyronel, Nathalie P de Leon, V Vuletić, and MD Lukin. Efficient fiber-optical interface for nanophotonic devices. *Optica*, 2(2):70–75, 2015.

[52] Michael J Burek, Charles Meuwly, Ruffin E Evans, Mihir K Bhaskar, Alp Sipahigil, Srujan Meesala, Bartholomeus Machielse, Denis D Sukachev, Christian T Nguyen, Jose L Pacheco, et al. Fiber-coupled diamond quantum nanophotonic interface. *Physical Review Applied*, 8(2):024026, 2017.

[53] Jeffrey Douglas Thompson, TG Tiecke, Nathalie P de Leon, J Feist, AV Akimov, M Gullans, Alexander S Zibrov, V Vuletić, and Mikhail D Lukin. Coupling a single trapped atom to a nanoscale optical cavity. *Science*, 340(6137):1202–1205, 2013.

[54] TG Tiecke, Jeffrey Douglas Thompson, Nathalie Pulmones de Leon, LR Liu, Vladan Vuletić, and Mikhail D Lukin. Nanophotonic quantum phase switch with a single atom. *Nature*, 508(7495):241–244, 2014.

[55] Lorenzo Magrini, Richard A Norte, Ralf Riedinger, Igor Marinković, David Grass, Uroš Delić, Simon Gröblacher, Sungkun Hong, and Markus Aspelmeyer. Near-field coupling of a levitated nanoparticle to a photonic crystal cavity. *Optica*, 5(12):1597–1602, 2018.

[56] Polnop Samutpraphoot, Tamara Dordević, Paloma L Ocola, Hannes Bernien, Crystal Senko, Vladan Vuletić, and Mikhail D Lukin. Strong coupling of two individually

controlled atoms via a nanophotonic cavity. *Physical Review Letters*, 124(6):063602, 2020.

[57] Je-Hyung Kim, Shahriar Aghaeimeibodi, Jacques Carolan, Dirk Englund, and Edo Waks. Hybrid integration methods for on-chip quantum photonics. *Optica*, 7(4):291–308, 2020.

[58] Ali Elshaari, Wolfram Pernice, Kartik Srinivasan, Oliver Benson, and Val Zwiller. Hybrid integrated quantum photonic circuits. *Nature Photonics*, 2020.

[59] Sara L Mouradian, Tim Schröder, Carl B Poitras, Luozhou Li, Jordan Goldstein, Edward H Chen, Michael Walsh, Jaime Cardenas, Matthew L Markham, Daniel J Twitchen, et al. Scalable integration of long-lived quantum memories into a photonic circuit. *Physical Review X*, 5(3):031009, 2015.

[60] Faraz Najafi, Jacob Mower, Nicholas C Harris, Francesco Bellei, Andrew Dane, Catherine Lee, Xiaolong Hu, Prashanta Kharel, Francesco Marsili, Solomon Assefa, et al. On-chip detection of non-classical light by scalable integration of single-photon detectors. *Nature communications*, 6(1):1–8, 2015.

[61] Iman Esmaeil Zadeh, Ali W Elshaari, Klaus D Jons, Andreas Fognini, Dan Dalacu, Philip J Poole, Michael E Reimer, and Val Zwiller. Deterministic integration of single photon sources in silicon based photonic circuits. *Nano Letters*, 16(4):2289–2294, 2016.

[62] Ryota Katsumi, Yasutomo Ota, Masahiro Kakuda, Satoshi Iwamoto, and Yasuhiko Arakawa. Transfer-printed single-photon sources coupled to wire waveguides. *Optica*, 5(6):691–694, 2018.

[63] AM Dibos, M Raha, CM Phenicie, and Jeffrey Douglas Thompson. Atomic source of single photons in the telecom band. *Physical review letters*, 120(24):243601, 2018.

[64] Je-Hyung Kim, Shahriar Aghaeimeibodi, Christopher JK Richardson, Richard P Leavitt, Dirk Englund, and Edo Waks. Hybrid integration of solid-state quantum emitters on a silicon photonic chip. *Nano letters*, 17(12):7394–7400, 2017.

[65] E Menard, KJ Lee, D-Y Khang, Ralph G Nuzzo, and John A Rogers. A printable form of silicon for high performance thin film transistors on plastic substrates. *Applied Physics Letters*, 84(26):5398–5400, 2004.

[66] Tommaso Pregnolato, Xiao-Liu Chu, Tim Schröder, Rüdiger Schott, Andreas D Wieck, Arne Ludwig, Peter Lodahl, and Nir Rotenberg. Deterministic positioning of quantum dots in nanophotonic waveguides. *arXiv preprint arXiv:1907.01426*, 2019.

[67] Gregory S MacCabe, Hengjiang Ren, Jie Luo, Justin D Cohen, Hengyun Zhou, Alp Sipahigil, Mohammad Mirhosseini, and Oskar Painter. Phononic bandgap nano-acoustic cavity with ultralong phonon lifetime. *arXiv preprint arXiv:1901.04129*, 2019.

[68] Chang-Ling Zou, Xu Han, Liang Jiang, and Hong X. Tang. Cavity piezomechanical strong coupling and frequency conversion on an aluminum nitride chip. *Phys. Rev. A*, 94:013812, Jul 2016.

[69] Amit Vainsencher, KJ Satzinger, GA Peairs, and AN Cleland. Bi-directional conversion between microwave and optical frequencies in a piezoelectric optomechanical device. *Applied Physics Letters*, 109(3):033107, 2016.

[70] RS Weis and TK Gaylord. Lithium niobate: summary of physical properties and crystal structure. *Applied Physics A*, 37(4):191–203, 1985.

[71] Flavius V. Pop, Abhay S. Kochhar, Gabriel Vidal-Álvarez, and Gianluca Piazza. Laterally vibrating lithium niobate MEMS resonators with 30% electromechanical coupling coefficient. In *Proceedings of the IEEE International Conference on Micro Electro Mechanical Systems (MEMS)*, pages 966–969. Institute of Electrical and Electronics Engineers Inc., feb 2017.

[72] Per Delsing, Andrew N Cleland, Martin JA Schuetz, Johannes Knörzer, Géza Giedke, J Ignacio Cirac, Kartik Srinivasan, Marcelo Wu, Krishna Coimbatore Balram, Christopher Bäuerle, et al. The 2019 surface acoustic waves roadmap. *Journal of Physics D: Applied Physics*, 52(35):353001, 2019.

[73] M Pijolat, A Reinhardt, E Defay, C Deguet, D Mercier, M Aid, JS Moulet, B Ghyselen, D Gachon, and S Ballandras. Large qxf product for hbar using smart cut$^{\text{TM}}$ transfer of linbo 3 thin layers onto linbo 3 substrate. In *2008 IEEE ultrasonics symposium*, pages 201–204. IEEE, 2008.

[74] BT Matthias and JP Remeika. Ferroelectricity in the ilmenite structure. *Physical Review*, 76(12):1886, 1949.

[75] Kenji Uchino. *Advanced piezoelectric materials: Science and technology*. Woodhead Publishing, 2017.

[76] D.P. Morgan. History of SAW devices. In *Proceedings of the 1998 IEEE International Frequency Control Symposium (Cat. No.98CH36165)*, pages 439–460. IEEE.

[77] Isaku Kanno. Piezoelectric mems: Ferroelectric thin films for mems applications. *Japanese Journal of Applied Physics*, 57(4):040101, 2018.

[78] Marc-Alexandre Dubois and Paul Muralt. Properties of aluminum nitride thin films for piezoelectric transducers and microwave filter applications. *Applied Physics Letters*, 74(20):3032–3034, 1999.

[79] K Fricke. Piezoelectric properties of gaas for application in stress transducers. *Journal of applied physics*, 70(2):914–918, 1991.

[80] DA Bryan, RR Rice, Robert Gerson, HE Tomaschke, KL Sweeney, and LE Halliburton. Magnesium-doped lithium niobate for higher optical power applications. *Optical Engineering*, 24(1):241138, 1985.

[81] Songbin Gong and Gianluca Piazza. Design and analysis of lithium-niobate-based high electromechanical coupling RF-MEMS resonators for wideband filtering. In *IEEE Transactions on Microwave Theory and Techniques*, volume 61, pages 403–414, 2013.

[82] Harmeet Bhugra and Gianluca Piazza. *Piezoelectric MEMS resonators*. Springer, 2017.

[83] Patricio Arrangoiz-Arriola, E. Alex Wollack, Marek Pechal, Jeremy D. Witmer, Jeff T. Hill, and Amir H. Safavi-Naeini. Coupling a Superconducting Quantum Circuit to a Phononic Crystal Defect Cavity. *Physical Review X*, 8(3):031007, jul 2018.

[84] Colin Campbell. *Surface Acoustic Wave Devices for Mobile and Wireless Communications, Four-Volume Set*. Academic press, 1998.

[85] Renyuan Wang, Sunil A. Bhave, and Kushal Bhattacharjee. High kt2, multi-frequency lithium niobate resonators. In *Proceedings of the IEEE International Conference on Micro Electro Mechanical Systems (MEMS)*, pages 165–168, 2013.

[86] Jouni V Knuuttila, Pasi T Tikka, and Martti M Salomaa. Scanning michelson interferometer for imaging surface acoustic wave fields. *Optics letters*, 25(9):613–615, 2000.

[87] Bertram Alexander Auld. *Acoustic fields and waves in solids*. Wiley Interscience Publications, 1973.

[88] Iren E Kuznetsova, Boris D Zaitsev, Shriniras G Joshi, and Irina A Borodina. Investigation of acoustic waves in thin plates of lithium niobate and lithium tantalate. *IEEE Transactions on Ultrasonics, Ferroelectrics, and Frequency Control*, 48(1):322–328, 2001.

[89] H. Nagata, N. Mitsugi, K. Shima, M. Tamai, and E. M. Haga. Growth of crystalline LiF on CF4 plasma etched LiNbO3 substrates. *Journal of Crystal Growth*, 187(3-4):573–576, may 1998.

[90] Marco Bazzan and Cinzia Sada. Optical waveguides in lithium niobate: Recent developments and applications. *Applied Physics Reviews*, 2(4):040603, 2015.

[91] Cheng Wang, Michael J. Burek, Zin Lin, Haig A. Atikian, Vivek Venkataraman, I-Chun Huang, Peter Stark, and Marko Lončar. Integrated high quality factor lithium niobate microdisk resonators. *Optics Express*, 22(25):30924, dec 2014.

[92] Mitsushi Itano, Frederick W. Kern, Masayuki Miyashita, and Tadahiro Ohmi. Particle Removal from Silicon Wafer Surface in Wet Cleaning Process. *IEEE Transactions on Semiconductor Manufacturing*, 6(3):258–267, 1993.

[93] Lutong Cai, Ashraf Mahmoud, and Gianluca Piazza. Low-loss waveguides on Y-cut thin film lithium niobate: towards acousto-optic applications. *Optics Express*, 27(7):9794, apr 2019.

[94] Christopher J. Sarabalis, Yanni D. Dahmani, Agnetta Y. Cleland, and Amir H. Safavi-Naeini. The role of resonance and bandgaps in high keff transducers. apr 2019.

[95] AO Oladipo, A Lucibello, M Kasper, S Lavdas, GM Sardi, E Proietti, F Kienberger, R Marcelli, and NC Panoiu. Analysis of a transmission mode scanning microwave microscope for subsurface imaging at the nanoscale. *Applied Physics Letters*, 105(13):133112, 2014.

[96] Songbin Gong and Gianluca Piazza. An 880 mhz ladder filter formed by arrays of laterally vibrating thin film lithium niobate resonators. In *2014 IEEE 27th International Conference on Micro Electro Mechanical Systems (MEMS)*, pages 1241–1244. IEEE, 2014.

[97] Amir H Safavi-Naeini, Dries Van Thourhout, Roel Baets, and Raphaël Van Laer. Controlling phonons and photons at the wavelength scale: integrated photonics meets integrated phononics. *Optica*, 6(2):213–232, 2019.

[98] Bradley A Moores, Lucas R Sletten, Jeremie J Viennot, and KW Lehnert. Cavity quantum acoustic device in the multimode strong coupling regime. *Physical review letters*, 120(22):227701, 2018.

[99] Emil Zeuthen, Albert Schliesser, Anders S Sørensen, and Jacob M Taylor. Figures of merit for quantum transducers. *Quantum Science and Technology*, 2020.

[100] DJ Wilson, Vivishek Sudhir, Nicolas Piro, Ryan Schilling, Amir Ghadimi, and Tobias J Kippenberg. Measurement-based control of a mechanical oscillator at its thermal decoherence rate. *Nature*, 524(7565):325–329, 2015.

[101] Andrew J Keller, Paul B Dieterle, Michael Fang, Brett Berger, Johannes M Fink, and Oskar Painter. Al transmon qubits on silicon-on-insulator for quantum device integration. *Applied Physics Letters*, 111(4):042603, 2017.

Appendix A

Extracting Transduction Parameters from a Transmission Measurement

In this appendix, coupled acoustic and optical modes are examined using a Quantum Langevin Equation (QLE) approach. We follow the reasoning of a similar calculation performed in Ref. [22]. First, we solve the acoustic cavity QLEs by assuming a weak optical mode. Then, we decompose the optical solution into a sum of sidebands around a carrier tone and solve the optical cavity QLEs. The solutions are used to relate the input microwave power to the strength of the beat note between the pump and resonant sideband signals. Finally, the single photon coupling g_0, microwave to optical photon number conversion efficiency $\eta_{\mu\to o}$, and other relevant figures-of-merit are calculated in terms of the scattering parameter S_{21} that we measure in our experiment.

We begin with Eqs. 3.10, 3.11, the equations of motion for an optical cavity (a) and an acoustic cavity (b)

$$\dot{a} = \Big(i\Delta - \frac{\kappa}{2}\Big)a - ig_0 a\Big(b + b^\dagger\Big) + \sqrt{\kappa_e}a_{in} \tag{A.1}$$

$$\dot{b} = -\Big(i\Omega_m + \gamma/2\Big)b - ig_0 a^\dagger a + \sqrt{\gamma_e}b_{in} \tag{A.2}$$

In our notation, a, b are annihilation operators of an optical cavity mode and an acoustic

mode, Ω_m is the resonant frequency of the acoustic mode, the detuning $\Delta = \omega_d - \omega_c$ is the difference between the drive frequency ω_d and the resonant frequency of the optical cavity ω_c, $\kappa = \kappa_i + \kappa_e$ is the total loss rate of the optical mode where κ_i, κ_e are the intrinsic and extrinsic optical loss rates, likewise $\gamma = \gamma_i + \gamma_e$ is the total loss rate of the acoustic mode where κ_i, κ_e are the intrinsic and extrinsic acoustic loss rates, g_0 is the single-photon coupling rate, and a_{in}, b_{in} are the input optical and microwave fields.

A single-frequency microwave drive $b_{in} = B_{in}e^{-i\Omega_d t}$ is applied at frequency Ω_d with amplitude B_{in}. The microwave input power is therefore defined as $P_{in} = \hbar\Omega_d|B_{in}|^2$. In our experiment we are in the weak optical mode limit $g_0 a^\dagger a \ll \Omega_m$ according to our reported values in Tab. 3.1. This allows us to neglect the optical back-action term $-ig_0 a^\dagger a$ in Eq. A.2, simplifying the equation into a first-order linear ODE. We plug in b_{in} and solve for b using an integrating factor

$$b = \frac{\sqrt{\gamma_e B_{in}}}{i(\Omega_m - \Omega_d) + \gamma/2} e^{-i\Omega_d t} = Be^{-i\Omega_d t} \tag{A.3}$$

where we define

$$B = \frac{\sqrt{\gamma_e B_{in}}}{i(\Omega_m - \Omega_d) + \gamma/2} \tag{A.4}$$

Next, we plug this result into Eq. A.1, where we find

$$\dot{a} = \Big(i\Delta - \frac{\kappa}{2}\Big)a - iGa\Big(e^{-i\Omega_d t} + e^{i\Omega_d t}\Big) + \sqrt{\kappa_e}a_{in} \tag{A.5}$$

where we have defined $G = g_0 B$

Our goal is to calculate the scattering parameter $S_{21} = \frac{P_{out}}{P_{in}}$, the ratio of the microwave output to input powers measured by the network analyzer. At this point we have an expression for P_{in} and we are interested in calculating P_{out}, the power recorded on our GHz frequency photodetector. The photodetector signal is the beat note between the optical drive tone and the cavity-enhanced sideband generated by the optomechanical interaction. We move forward by decomposing the optical amplitude a into a sum of sidebands

$$a = \sum_{q=0} A_q e^{-iq\Omega_d t} \tag{A.6}$$

where A_q is the amplitude of the order q sideband. We drop all but three of these terms by assuming that only the carrier A_0 and first order sidebands are significant. We justify

this assumption by noting that we are in the weak microwave mode limit $G \ll \kappa$ and we are in the near sideband resolved regime $\Omega_m \approx \kappa$. We also confirmed that power in the higher order sidebands is negligible experimentally. We re-label $A_1 \rightarrow A_+,\ A_{-1} \rightarrow A_-,\ a_{in} \rightarrow A_{in}$ and plug Eq. A.6 into Eq. A.5. Grouping the terms by sideband, we find

$$\begin{aligned} 0 &= \Big(i\Delta - \frac{\kappa}{2}\Big)A_0 - iG\Big(A_+ + A_-\Big) + \sqrt{\kappa_e}A_{in} \\ -\Omega_d A_+ &= \Big(i\Delta - \frac{\kappa}{2}\Big)A_+ - iGA_0 \\ \Omega_d A_- &= \Big(i\Delta - \frac{\kappa}{2}\Big)A_- - iGA_0 \end{aligned} \tag{A.7}$$

The solution to this system of equations is easily found.

$$\begin{aligned} A_0 &= \frac{\sqrt{\kappa_e}A_{in}}{\Big(i\Delta + \kappa/2 + G^2(\frac{1}{i(\Delta-\Omega_d)+\kappa/2} + \frac{1}{i(\Delta+\Omega_d)+\kappa/2})\Big)} \\ A_+ &= \frac{-iGA_0}{i(\Delta+\Omega_d)+\kappa/2} \\ A_- &= \frac{-iGA_0}{i(\Delta-\Omega_d)+\kappa/2} \end{aligned} \tag{A.8}$$

We operate in the case where the laser is blue-detuned from the optical resonance by the mechanical resonance frequency ($\Delta = \Omega_m$) and the microwave drive is set to the mechanical resonance frequency ($\Omega_d = \Omega_m$). This simplifies our equations and leads to an enhancement of the sideband A_-, which is resonant with the optical cavity frequency.

$$\begin{aligned} A_0 &\approx \frac{\sqrt{\kappa_e}A_{in}}{\Big(i\Omega_m + \kappa/2\Big)} \\ A_- &= \frac{-iGA_0}{\kappa/2} = \frac{-iG\sqrt{\kappa_e}A_{in}}{\kappa/2\Big(i\Omega_m + \kappa/2\Big)} \end{aligned} \tag{A.9}$$

Setting ($\Omega_d = \Omega_m$) also simplifies Eq. A.4 to $B = 2\sqrt{\gamma_e}B_{in}/\gamma$. We also note that when the laser is detuned from the cavity, we can assume that almost all drive light is reflected off of the cavity and indecent on the fast photodiode with amplitude $\approx A_{in}$.

A given photodetector has a responsivity R_{PD} the ratio of output voltage to input power, given in units of V/W. The beat note of the drive light the resonant sideband generates an output microwave voltage U on the fast photodiode, given by

$$
\begin{aligned}
U &= R_{PD}\hbar\omega_d|\sqrt{\kappa_e}A_{in}A_-| \\
U &= R_{PD}\hbar\omega_d|A_{in}|^2\frac{\kappa_e G}{\kappa/2\left(\sqrt{\Omega_m^2+\kappa^2/4}\right)}
\end{aligned}
\tag{A.10}
$$

where we plugged in Eq. A.9 in the second line. We continue working on A.10 by defining the optical power received at the photodiode $I_{Rec} = \hbar\omega_d|A_{in}|^2$ and remembering that our device is in the near resolved sideband.

$$
U \approx R_{PD}I_{Rec}\frac{2\kappa_e G}{\kappa\Omega_m} \tag{A.11}
$$

Then, we relate the microwave voltage received by the photodetector to the power received by the network analyzer output port $P_{out} = \frac{U^2}{2R_{Load}}$, where R_{Load} is the impedance of the port. We find

$$
P_{out} = \frac{2G^2\kappa_e^2 R_{PD}^2 I_{Rec}^2}{\Omega_m^2\kappa^2 R_{Load}} \tag{A.12}
$$

Finally, we can calculate S_{21}. Recall that $P_{in} = \hbar\Omega_m B_{in}^2$ and $G = g_0 B = 2g_0\sqrt{\gamma_e}B_{in}/\gamma$.

$$
\begin{aligned}
S_{21} &= \frac{P_{out}}{P_{in}} \\
S_{21} &= \frac{8g_0^2\gamma_e\kappa_e^2 R_{PD}^2 I_{Rec}^2}{\hbar\gamma^2\Omega_m^3\kappa^2 R_{Load}}
\end{aligned}
\tag{A.13}
$$

The second line is Eq. 3.13, which we used in the text to calculate g_0 from experimentally available values. Using g_0 we want to calculate the photon number conversion efficiency $\eta_{\mu\to o}$, defined as the number of output optical sideband photons per input microwave photons. We also define I_{In} as the optical power input to the optical cavity. The result is

$$
\begin{aligned}
\eta_{\mu\to o} &= \left|\frac{\sqrt{\kappa_e}A_-}{B_{in}}\right|^2 \\
\eta_{\mu\to o} &= \frac{16g_0^2\gamma_e\kappa_e^2 I_{in}}{\hbar\omega_c\Omega_m^2\kappa^2\gamma^2} \\
\eta_{\mu\to o} &= \frac{4g_0^2}{\gamma\kappa}\cdot\frac{\kappa_e I_{In}}{\Omega_m^2\hbar\omega_o}\cdot\frac{2\gamma_e}{\gamma}\cdot\frac{2\kappa_e}{\kappa}
\end{aligned}
\tag{A.14}
$$

The third line is Eq. 3.14, which allows us to derive our second important figure-of-merit from the measurement in Section 3.4.